

This revised manuscript – a preprint submitted to  
EarthArXiv – is in peer-review with the journal  
QUATERNARY SCIENCE REVIEWS.

Please note that the manuscript is under revision and  
subsequent versions of this research article may have a  
slightly different content.

If accepted, the final version of the manuscript will be  
available via the “Peer-reviewed Publication DOI” link on  
this webpage.

1 **Environmental variability at the margin of the South American Monsoon**  
2 **System recorded by a high-resolution sediment record from Lagoa Dourada**  
3 **(South Brazil)**

4

5 Bernd Zolitschka\*<sup>1</sup>, An-Sheng Lee<sup>1,2</sup>, Daniela Piraquive Bermúdez<sup>3</sup>, Thomas Giesecke<sup>3,4</sup>

6

7 <sup>1</sup>University of Bremen, Institute of Geography, Germany

8 <sup>2</sup>National Taiwan University, Department of Geosciences and Research Center for Future Earth,  
9 Taipei, Taiwan

10 <sup>3</sup>Department of Palynology and Climate Dynamics, University of Göttingen, Germany

11 <sup>4</sup>Department of Physical Geography, Utrecht University, The Netherlands

12 \*Corresponding author: University of Bremen, Institute of Geography, Celsiusstr. 2, 28259 Bremen,  
13 Germany (E-Mail: zoli@uni-bremen.de)

14

15 **ORCID's**

16 BZ: <https://orcid.org/0000-0001-8256-0420>

17 ASL: <https://orcid.org/0000-0002-5492-1986>

18 DPB: <https://orcid.org/0000-0002-7686-8135>

19 TG: <https://orcid.org/0000-0002-5132-1061>

20

21 **Keywords:** hydroclimate, soil erosion, human impact, XRF scanning, geochemistry, Holocene, 8.2 ka  
22 event, 4.2 ka event, Little Ice Age, South American Monsoon System (SAMS)

23

24 **Abstract**

25 High-resolution geochemical and sedimentological data have been obtained for a lacustrine sediment  
26 record from Lagoa Dourada (South Brazil). Four distinctly different depositional processes were  
27 determined: (1) Suspension fallout of fine-grained minerogenic particles transferred via fluvial  
28 activity dominates the Early Holocene and relates to open grassland in the catchment area; (2)  
29 Activation of the karst hydrological system with deposition of massive sand layers indicates increased  
30 precipitation at the onset of the Middle Holocene; (3) Minerogenic sediments are replaced by  
31 organic deposition due to wetter climatic conditions with the expansion of woodlands in combination  
32 with release of dissolved nutrients due to enhanced pedogenesis during the Middle to Late  
33 Holocene; (4) Human-induced land-use change caused destabilization of soils in the catchment area  
34 with resulting cultural soil erosion between AD 1800 and 1950. These depositional trends are linked  
35 to intensity variations of the South American Monsoon System (SAMS). Century-long climatic events  
36 detected by data of high-resolution XRF scanning confirm this relationship and provide signals of the

37 8.2 and 4.2 ka events as well as of the Little Ice Age. These events document increased rainfall with  
38 complex responses of the environmental system. Our SAMS-induced consequences of past  
39 hydroclimatic variability on the environment of South Brazil provide background information for  
40 better evaluating model projections of future climate change.

41

## 42 **Introduction**

43 Brazil is the country with the second largest forest cover in the world and thus provides an enormous  
44 potential for decarbonization initiatives through CO<sub>2</sub> storage in biomass. Especially, the Amazon and  
45 the Atlantic rain forests belong to those regions on Earth with the richest biodiversity (Carnaval et al.,  
46 2009; Myers et al., 2000). Moreover, the Atlantic rain forest was and is very important for the  
47 economic development of Brazil. Where once forests were growing, there is today rapid  
48 industrialization hosting one of the most densely populated regions of South America. Most forests  
49 disappeared, with less than 10 % remaining as fragmented woodlands. This has major consequences  
50 for regional climate, biodiversity and soil erosion (Freitas, 2011).

51 The Atlantic rain forest is a 4000 km long and 100-200 km wide band along the Atlantic coast of  
52 Brazil, from tropical Natal in the NE (5 °S) to subtropical Porto Alegre in the S (30 °S). Its appearance  
53 is dependent on the spatial and temporal distribution of precipitation and climatologically controlled  
54 by the South American Monsoon System (SAMS) (Deininger et al., 2019; Zhou and Lau, 1998).  
55 Moreover, this is the most significant atmospheric circulation system of South America and  
56 responsible for precipitation from the Amazon to the La Plata Basin (Baker and Fritz, 2015). This  
57 large-scale climatic system is driven by differential heating of continents and oceans and responsible  
58 for seasonal reversals of low-level winds, a typical monsoon feature (Zhou and Lau, 1998). In  
59 southern winter, the Intertropical Convergence Zone (ITCZ) remains north of the equator, while SE  
60 Brazil is dominated by the South Atlantic high-pressure cell moving towards the continent. Thus, the  
61 advection of cold polar air masses closely linked to South Atlantic cyclones (SACs) brings humidity  
62 from the Atlantic Ocean to South America with coastal rainfall from 25-30°S. At the same time, NE  
63 Brazil experiences a dry season of 6-8 months duration. This constellation changes in southern  
64 summer, when the ITCZ extends further to the south. Warm and moist tropical air masses from the  
65 Amazon Basin cause rainfall from 15-25 °S, while the Atlantic high-pressure cell is weakened and  
66 moves to an offshore position (Baker and Fritz, 2015; Ledru et al., 1998). Currently, 60 % of  
67 precipitation is related to the summer monsoon (October-March) and 40 % are considered as winter  
68 rain (Cruz et al., 2007). Most of the millennial-scale variability of the SAMS coincides with orbital  
69 forcing, i.e. variations of insolation, while minor influences are related to Southern Hemispheric  
70 Westerlies (SHW) and Atlantic sea surface temperatures (Baker and Fritz, 2015; Deininger et al.,  
71 2019; Utida et al., 2020). As the Atlantic rain forest depends on the amount of precipitation, orbitally  
72 controlled changes in precipitation are directly linked to its retractions and expansions but also to  
73 changes in vegetation types, i.e. from grasslands to woodlands and vice versa (Ledru et al., 2009;  
74 Novello et al., 2017).

75 Such climatic changes are not directly recorded in environmental archives but have to be inferred  
76 from the results of environmental processes acting under particular climate conditions. These proxy  
77 data are usually imperfect recorders of a small number and often not well constrained climate and  
78 environmental variables. In this regard, lake sediments are considered one of the most powerful  
79 terrestrial archives of past environmental and hydroclimatic variability. Such information is also an  
80 important contribution to the understanding of present ecosystems and their stability. Through a  
81 large number of proxies, lake sediment records have the potential to characterize their lacustrine  
82 system and the catchment area with natural and anthropogenic processes closely linked to regional  
83 hydroclimatic conditions. However, and due to the scarce occurrence of natural lakes in S and SE  
84 Brazil, only a limited number of such long-term environmental histories are available. Just three

85 multiproxy studies were carried out on lacustrine sediments that include geochemical,  
86 sedimentological, diatom and/or stable isotope data and provide a more comprehensive picture of  
87 environmental processes: Lago Aleixo at 18 °S (Enters et al., 2010), Lago Silvana at 19.5 °S (Rodrigues-  
88 Filho et al., 2002) and Lagoa Dourada at 25 °S (Melo et al., 2003; Moro et al., 2004). The majority of  
89 paleoenvironmental investigations carried out in this SAMS-dominated region are pollen and  
90 charcoal studies of small wetlands mainly from highlands and coastal mountains (Rodrigues et al.,  
91 2016) and only a small number of studies reconstructing Holocene and Late Pleistocene vegetation is  
92 based on lacustrine sediments (e.g., Behling, 1995, 2003; Behling and Safford, 2009).

93 The best available information on hydrological changes in S Brazil is provided by the speleothem  
94 records from Caverna Botuverá (Bernal et al., 2016b; Cruz et al., 2005). Their oxygen isotope records  
95 document a period of increased humidity during the Younger Dryas (YD), while the remainder of the  
96 Late Glacial and the Early Holocene were dry relative to present-day conditions. At that time, the  
97 vegetation on highlands and coastal mountains was dominated by grasslands with the  
98 Pleistocene/Holocene transition often marked by a shift in abundance of fern spores, possibly  
99 responding to the more humid YD (Behling and Oliveira, 2017; Behling et al., 2004). These relatively  
100 dry conditions of the Early Holocene caused hillslope denudation with silt-rich suspension deposits in  
101 lakes as reported e.g. for Lago Silvana (Rodrigues-Filho et al., 2002).

102 The oxygen isotope record indicates a shift to more humid conditions between 7000 and 4400 cal. BP  
103 (Bernal et al., 2016b; Cruz et al., 2009) and many pollen diagrams from S and SE Brazil indicate a  
104 gradual increase in woodland cover across the highlands (e.g., Behling et al., 2004; Jeske-Pieruschka  
105 et al., 2013). Thus, hillslope erosion was more and more reduced and chemical weathering increased  
106 leading to intensified pedogenesis with the leaching of nutrients. Consequently, the surplus of  
107 nutrients enhanced the biological productivity of lakes as documented by organic sediments e.g. for  
108 Lago Aleixo (Enters et al., 2010). A major spread of woodlands and in particular of *Araucaria*  
109 *angustifolia* in pollen diagrams started only after ca. 4300 cal. BP with marked increases at 2800 and  
110 1200 cal. BP leading to the development of the modern mosaic of grasslands and *Araucaria* forests  
111 (Rodrigues et al., 2016). These conditions continued until the last millennium when few pollen  
112 records document even wetter climatic conditions, i.e. they are evidence for the Little Ice Age (LIA)  
113 (Behling, 2003; Behling et al., 2004). Finally, the vegetation was modified by agricultural activities of  
114 European settlers that started in the late 18<sup>th</sup> century increasing thereafter (Freitas, 2011). In  
115 consequence, soil erosion was activated leading to deposition of more minerogenic sediments in  
116 some of the studied lakes (Enters et al., 2010; Portes et al., 2018).

117 Located at the southern fringe of SAMS influence, Lagoa Dourada is a promising site to enhance our  
118 understanding of Holocene climatic conditions with high-resolution environmental records. Initial  
119 low-resolution investigations are available, including palynological, diatom, total carbon,  $\delta^{13}\text{C}$ , LOI-  
120 550 as well as selected elemental (P, Ca, Mg, K) data (Lorscheitter and Takeda, 1995; Melo et al.,  
121 2003; Moro et al., 2004). However, the provided chronology is based on only two bulk radiocarbon  
122 dates from the Early Holocene, insufficient for a detailed understanding of paleoenvironmental  
123 changes. With this investigation, we provide new and high-resolution sedimentological and  
124 geochemical data to study hydroclimatic variations from a site located in a climatically sensitive  
125 region of S Brazil. Thirty years after first investigations at Lagoa Dourada have been carried out (Melo  
126 et al., 2003; Moro et al., 2004), this lake was re-visited and two long and overlapping sediment  
127 profiles were recovered. The major goal of this study focuses on the knowledge gap existing for low-  
128 and high-frequency environmental variability in SE Brazil climatically controlled by the SAMS.  
129 Moreover, we aim at providing detailed background information to better evaluate past climatic  
130 developments, which provide keystones for model predictions of future climatic conditions. To  
131 achieve this goal, we use sophisticated age-depth modeling based on radiocarbon-dated terrestrial  
132 macro remains and on bulk dates with reservoir correction, apply scanning techniques (X-ray  
133 fluorescence, magnetic susceptibility) as well as multiproxy sediment analyses to establish a

134 continuous and high-resolution geochemical and sedimentological dataset for a better understanding  
135 of the responses of lacustrine and geomorphological systems to hydroclimatic variability.

136 Furthermore, anthropogenic impacts of the last two centuries are discussed that influence cultural  
137 soil erosion and lacustrine eutrophication. This is supported by high-resolution investigations of  
138 pollen and charcoal reliably linking vegetation and forest fires to climatic variations and human  
139 activities. Except for pollen and charcoal studies, which are discussed by Piraquive Bermúdez (2020)  
140 and will be published elsewhere, this investigation provides a comprehensive and well-dated  
141 multiproxy investigation allowing insights into geomorphological processes in the catchment area as  
142 well as into lacustrine processes, all reflecting hydroclimatic fluctuations in response to SAMS  
143 variability during the Holocene.

144

## 145 **Study Site**

146 Lagoa Dourada (Portuguese: Golden Lake) is located in Vila Velha State Park near Ponta Grossa  
147 (25°14'25" S, 50°02'59" W, 817 m asl) around 80 km W of Curitiba, the capital of the State of Paraná  
148 (S Brazil), and 180 km W of the Atlantic coast. The small lake has a maximum water depth of 5.4 m  
149 and is elliptical in shape with a size of ca. 150 m x 200 m (Moro et al., 2004). It was formed in the  
150 Furnas Formation on the Second Paraná Plateau (Fig. 1). The Furnas Formation is of Silurian to  
151 Devonian age, part of the Paleozoic Paraná Sedimentary Basin, mainly consists of whitish, medium to  
152 coarse-grained quartzitic sandstones (Melo and Giannini, 2007; Pires et al., 2019) and is classified as  
153 quartz-arenite with 97 % quartz (Pontes et al., 2020). Aside from mainly kaolinite as cement, these  
154 sandstones are enriched in ultra-stable minerals such as zircon (Moro et al., 2004). Chemical  
155 weathering of the cement as well as of quartz-grain surfaces by intergranular corrosion is responsible  
156 for the process of arenization, which loosens and removes sand grains by groundwater (Wray, 2013).  
157 Overall, arenization increases the underground porosity and finally causes the development of  
158 silicate karst.

159 The Vila Velha State Park was created in 1953 and is enlisted as a State Heritage since 1966 (Thomaz,  
160 2010). It is famous for its karstic features in sandstone with caves, dolines, sinkholes, speleothems,  
161 karren, collapse structures and underground drainage systems including karstic springs (Melo and  
162 Giannini, 2007). The formation of quartzitic karst is very slow-acting compared to carbonaceous karst  
163 and requires extended periods of geological stability with intensive chemical weathering. As a  
164 consequence of subterranean karstic erosion, Lagoa Dourada was formed as a sinkhole after the roof  
165 of a cave collapsed. Such sinkholes (Portuguese: furnas) are typical for this part of the Paraná Basin  
166 and eponymous for the Paleozoic Furnas Formation.

167 As the non-fluvial catchment area of Lagoa Dourada is composed of siliceous karst, there is limited  
168 surface runoff into the lake: precipitation immediately infiltrates, contributes to the underground  
169 karstic drainage system and returns to the surface via layered karstic springs at the northern shores  
170 of Lagoa Dourada. There the Furnas Formation borders the alluvial plain of Rio Guabiroba.  
171 Petrographic data document that sands transferred via karstic springs are enriched in ultra-stable  
172 minerals like their source: the Furnas Formation (Melo et al., 2003).

173 The short and ca. 300 m-long outflow of Lagoa Dourada drains into Rio Guabiroba. However, during  
174 high rainfall events with flooding, the water in the outflow channel changes direction and enters the  
175 lake. These floodwater invasions are silting-up Lagoa Dourada from the S, while the largest water  
176 depth of the lake is close to the northern shore (Melo et al., 2003). During flooding, a much larger  
177 catchment area extends ca. 25 km towards E (Fig. 1). This watershed of Rio Guabiroba includes not  
178 only sandstones of the Furnas Formation but also shales and fine-grained sandstones of the  
179 Devonian Ponta Grossa Formation as well as reddish and predominantly medium-grained Vila Velha  
180 Sandstones of the Upper Carboniferous Itararé Group (Fig. 1). The latter is cemented by iron and

181 manganese oxides and dominated by quartz with a high mineralogical maturity (Melo et al., 2003;  
182 Melo and Coimbra, 1996). Some of the strongly cemented parts of the Vila Velha Sandstone are  
183 resistant against weathering and form ruined inselbergs described as “ruiniform relief” (Melo and  
184 Coimbra, 1996), one of the major attractions of the Vila Velha State Park.

185 The subtropical climate at Vila Velha is characterized by temperate oceanic conditions without dry  
186 seasons (Cfb according to the Köppen classification). The mean annual temperature is 17.5 °C  
187 (warmest month January: 21.4 °C; coldest month July: 13.7 °C) and the annual sum of precipitation  
188 reaches 1495 mm (wettest month February: 177 mm; driest month August: 83 mm) (Merkel, 2020).  
189 Regional vegetation is dominated by subtropical grassland (Campos) with *Araucaria* woodlands  
190 covering hills and valleys (Moro and Fürstenberger, 1998). A recent vegetation map of the Vila Velha  
191 State Park determined *Araucaria angustifolia* (12 %) as the characteristic local tree in valleys and  
192 moister habitats with deeper soils, while on shallow and drier soils on sandstones Campos dominates  
193 with Poaceae (23 %), Cyperaceae (13 %), Asteraceae (10 %) and *Baccharis* (9 %) (Piraquive Bermúdez  
194 et al., 2021).

195 The modern freshwater of Lagoa Dourada is characterized by alkalinity of 77.5 mg/l, pH of 7.8, water  
196 temperature of 19.8 °C and 9.2 mg/l dissolved oxygen. All measurements are mean August values  
197 obtained from the epilimnion of 1990-1993 (Moro and Fürstenberger, 1998). These water conditions  
198 are confirmed by modern diatom samples, which document eutrophic conditions typical for a  
199 shallow alkaline to neutral lake with a dominance (>90 %) of periphytic over planktonic diatom  
200 species (Moro and Fürstenberger, 1998).

201

## 202 **Methods**

### 203 Coring, lithological description and subsampling

204 In February 2017 two parallel and overlapping sediment cores (LD17-A: to a sediment depth of 14.0  
205 m; LD17-B: 14.2 m) have been recovered. The upper 10 m were cored with a light-weight Livingstone  
206 piston corer (Nesje et al., 1987) and the deeper sediments with a square-rod Livingstone piston corer  
207 (Wright, 1967). The 1 m long core sections (diameter: 50 mm) were obtained from a location south of  
208 the largest water depth (5.4 m) of Lagoa Dourada (50°2'58.21" W; 25°14'25.55" S). Coring sites were  
209 10-15 m apart and at 4.0 m (LD17-A) and 2.8 m (LD17-B) water depths (Fig. 1). The upper 20 cm of  
210 the record were almost liquid, difficult to retain and only used for pollen analysis. All sediment cores  
211 were shipped to the University of Göttingen, where they were split, photographed and described  
212 macroscopically. In addition, 14 smear slides from characteristic intervals were prepared following  
213 Rothwell (1989) for microscopic sediment description (magnification: 100-400 x) at the University of  
214 Bremen. In support of core description, high-resolution color images are available from the line-scan  
215 camera mounted to the ITRAX X-ray fluorescence (XRF) core-scanner (Croudace et al., 2019;  
216 Croudace et al., 2006).

217 Subsampling for pollen (Piraquive Bermúdez, 2020) and in parallel for sedimentology and  
218 geochemistry (this study) was carried out providing a total of 177 samples with a mean spatial  
219 resolution of 8 cm.

### 220 Dating

221 Terrestrial plant macro remains, encountered during subsampling and searched for by sieving  
222 sediment slices, were preferably used for radiocarbon dating wherever possible. However, no  
223 macroscopic plant remains were found below 7.31 mcd (meter composite depth), except for a part of  
224 a twig at 9.24 mcd. Twenty-one AMS <sup>14</sup>C samples were dated at the Poznań Radiocarbon Laboratory  
225 in Poland (POZ) and two additional samples at the <sup>14</sup>Chrono Centre, Queen’s University Belfast in

226 Northern Ireland (UBA). Eight dates derive from terrestrial plant macro remains, while other  
227 determinations are based on bulk organic matter (OM; Tab. 1). To assess the magnitude of a  
228 presumed old carbon effect of bulk dates (reservoir effect), two sediment samples were submitted  
229 for radiocarbon dating above and below the terrestrial macrofossil date at 7.31 mcd. These two  
230 dates were not used in building the age model. In addition to the radiocarbon dates, the  
231 sediment/water interface (AD 2017) is used as a control point, while distinct sand sections in the core  
232 are interpreted as events and treated as instantaneous. Sediment accumulation in relation to the  
233 results of radiocarbon measurements and the core top was modelled using the R-package “rbacon”  
234 (Blaauw et al., 2021). Radiocarbon dates were calibrated during age modelling applying the Southern  
235 Hemisphere calibration curve SHCal20 (Hogg et al., 2020).

236 Several publications used for discussion provide only uncalibrated radiocarbon ages. To improve  
237 comparisons with our data, these ages were calibrated using OxCal 4.4 (Bronk Ramsey, 2009)  
238 applying the Southern Hemisphere calibration curve SHCal20 (Hogg et al., 2020).

### 239 Core scanning

240 Prior to applying non-destructive core scanning techniques, the split core halves were cleaned and  
241 smoothed. A continuous log of volume-specific magnetic susceptibility (MS) was measured in 1 cm  
242 increments with a Bartington MS2E sensor employed to an automated measuring bench (Dearing,  
243 1994; Nowaczyk, 2001). For analyzing the geochemical composition of sediment cores in high  
244 resolution, all sections were scanned with the ITRAX XRF core scanner (Cox Analytics) (Croudace et  
245 al., 2019; Croudace and Rothwell, 2015). The molybdenum (Mo) tube was used with constant  
246 settings of 30 kV and 50 mA, a step size of 2 mm and an exposure time of 5 s. The output was  
247 processed with the software Q-spec (Cox Analytics) and results are expressed in counts (cts), which  
248 describe relative intensities of 23 elements as well as variations of coherent (coh) and incoherent  
249 (inc) scattering.

250 In a next step, reproducibility of XRF elemental data was evaluated by five repeated scans of two 1 m  
251 long sections representing highly organic (sediment core LD17-B6) and highly minerogenic (LD17-  
252 B12) sediment with the same adjustments as mentioned above. A feasible way to evaluate the  
253 credibility of each determined element is to calculate correlation coefficients for elements between  
254 replicate measurements where high correlations indicate good reproducibility for the respective  
255 element. This procedure allows excluding elements with low signal-to-noise ratios (Löwemark et al.,  
256 2019), thus reducing the number of elements for statistical evaluation.

257 Due to changing physical properties along the sediment record, like matrix effects related to  
258 variations in water content, OM content and/or grain size, the chemical composition obtained by XRF  
259 core scanning is non-linearly correlated to element concentrations (Croudace et al., 2019; Tjallingii et  
260 al., 2007). Moreover, element intensities underlie the closed-sum effect, which inhibits multivariate  
261 statistical analyses (e.g., Martin-Puertas et al., 2017). A solution for these limiting factors is available  
262 with the centered log-ratio (clr), which normalizes data and determines relative changes in element  
263 composition resembling their chemical composition (Tjallingii et al., 2007; Weltje et al., 2015; Weltje  
264 and Tjallingii, 2008). Moreover, clr transformation is consistent with the statistical theory of  
265 compositional data analyses (Aitchison, 1982; Weltje et al., 2015) and calculates as:

$$266 \text{clr of } I_{ij} = \ln(I_{ij} / gm_j),$$

267 where  $I_{ij}$  is the intensity (I) of the element  $i$  for measurement  $j$  and  $gm_j$  is the geometric mean of all  
268 elements analyzed at measurement  $j$ . In addition to elemental clr values, we calculate the log  
269 molybdenum incoherent/coherent scattering ratio ( $\ln \text{inc/coh}$ ), which is regarded as a proxy for OM  
270 content of lacustrine sediments (Liu et al., 2013; Woodward and Gadd, 2019). This ratio of Compton  
271 scattering (inc) versus Rayleigh scattering (coh) depends on the presence of light elements (H, C, N,  
272 O). High amounts of these elements, such as analyzed for OM and/or high-water content, increase

273 the Compton Effect and thus the value for  $\ln \text{inc/coh}$ . Other possible matrix effects are negligible  
274 (Weltje and Tjallingii, 2008; Woodward and Gadd, 2019).

#### 275 Elemental analyses

276 Total carbon (TC), total nitrogen (TN) and total sulphur (TS) were measured with a CNS elemental  
277 analyzer (EuroEA, Eurovector). Prior to measurements, all 177 samples were freeze-dried, ground,  
278 homogenized and 5-20 mg were weighted into tin crucibles. During measurements, the elemental  
279 analyzer combusts the crucibles with the sample material at a temperature of 1800 °C. All OM is  
280 oxidized and the resulting gases ( $\text{CO}_2$ ,  $\text{NO}_2$ ,  $\text{SO}_2$ ) are detected by chromatography. As TC includes  
281 organic as well as inorganic carbon, a second step is necessary to distinguish total organic carbon  
282 (TOC) from total inorganic carbon (TIC). As the catchment area has no carbonaceous rocks, we  
283 assume that also the lacustrine sediments are carbonate-free. To test this hypothesis, 10 samples  
284 with TC values >2 % were treated first with 3 % and then with 20 % HCl at 80 °C to remove potential  
285 carbonates prior to measurement of TOC with the same elemental analyzer. Total inorganic carbon  
286 (TIC) was then calculated as the difference between TC and TOC. Furthermore and to distinguish  
287 autochthonous from allochthonous sources of OM, C/N ratios were calculated with low values (<10)  
288 indicative of autochthonous lacustrine productivity (algal matter), while higher values (>20) are  
289 dominated by higher plants with cellulose of terrestrial origin (Meyers and Teranes, 2001). Biogenic  
290 matter is calculated as the sum of opal (BSi) and OM, which is the product of TOC with the factor of  
291 2.13 (Dean, 1974).

292 Biogenic silica (BSi) was analyzed for 177 samples following the leaching method of Müller and  
293 Schneider (1993). We extracted BSi with 1M NaOH at 85 °C. The solution was cycled by a continuous-  
294 flow system into an auto analyzer, where dissolved silicon was detected by spectrophotometry.

#### 295 Grainsize

296 Prior to grainsize analysis, OM was removed by  $\text{H}_2\text{O}_2$  from each of the 177 samples. For dispersion,  
297 20 ml of Calgon [ $(\text{NaPO}_3)_n$ ] was added and agitated overnight. On the next day, analyses were  
298 performed with a laser diffraction analyzer (Beckman Coulter LS 200) after ultrasonic treatment for  
299 30 s. Each sample was measured at least four times for 60 s until a stable distribution was reached.  
300 Thereafter, the arithmetic mean was calculated for the best three sample runs. Grainsize  
301 distributions and all statistical grainsize parameters were calculated from the output of the LS 200 as  
302 geometric graphical measures according to Folk and Ward (1957) with the MS Excel-based macro  
303 Gradistat, Version 8.0 (Blott and Pye, 2001).

#### 304 Multivariate statistics

305 Principal component analysis (PCA) was applied to the standardized and normalized (clr-  
306 transformed) dataset obtained by XRF core scanning for reducing the data dimension (Abdi and  
307 Williams, 2010). The standardization rescaled each element's profile to zero mean and unit standard  
308 deviation. The selection of credible principal components (PCs) is based on the elbow concept and  
309 preference is given to PCs with >10 % of total variance. The first two PCs were selected and whitened  
310 (i.e., standardized) as data representation. The logic of whitening is the same as for standardization  
311 prior to PCA. The process of whitening gives the two selected PCs equal contribution for later  
312 clustering. We applied "hierarchical density-based spatial clustering of applications with noise"  
313 (HDBSCAN). This clustering algorithm combines hierarchical clustering with the spatial density metric  
314 of data and tends to find clusters with dense distributions (McInnes et al., 2017). Due to density-  
315 based characteristics, the shapes of the clusters are not limited to sphere-like shapes but can also be  
316 polygons as long as data points within these clusters are dense enough. Furthermore, data points  
317 located in a loose manner or at distance from the cores of dense clusters will be recognized as noise,  
318 i.e. as outlying data. This makes the algorithm robust against noise. HDBSCAN's hierarchical  
319 clustering approach on density metric provides flexibility with regard to density. In other words, data



320 points determined as dense clusters can be based on different densities, for details see the  
321 algorithm's source documents (<https://hdbscan.readthedocs.io/en/latest/index.html>). Two primary  
322 parameters have to be adjusted for this algorithm. `Min_cluster_size` sets the minimum size for the  
323 grouping of data considered as a cluster and `Min_sample` determines what the algorithm defines as  
324 "dense", i.e. how many data points will be selected as noise. A grid search for optimal parameters  
325 (`min_cluster_size`: 20, 50, 80, 100, 150, 200; `min_sample`: 2, 3, 4, 5, 8, 10) was carried out by  
326 checking the visualization of spatial data distributions on the first two PCs. Optimal `min_cluster_size`  
327 and `min_sample` were set to 100 and 5, respectively. Computations and part of visualizations were  
328 conducted using the packages in the Scipy ecosystem (Harris et al., 2020; Hunter, 2007; Pedregosa et  
329 al., 2011; van der Walt et al., 2014; Virtanen et al., 2020) and the HDBSCAN library (McInnes et al.,  
330 2017).

331 Individual cluster labels were smoothed to develop the clusterlog. This was carried out by looking at  
332 subsets of 11 consecutive data points (11 x 2 mm). For each of these subsets, fragmented labels and  
333 labels of minor importance were replaced by the dominant label. Thus, 31.4 % of noise was changed  
334 to cluster labels, which increased the number of cluster labels for all clusters except for cluster 3,  
335 which remained unchanged.

336

## 337 **Results**

### 338 Core correlation and lithological description

339 Correlation of core sections from LD17-A and LD17-B is based on 20 marker layers clearly  
340 distinguishable on high-resolution line-scan images and supported by high-resolution XRF core  
341 scanning data. Of all detected elements, Ca is best suited for this purpose due to relatively high  
342 counts combined with sufficient variability along the entire record (Fig. S1). All depths of the  
343 established composite record are provided in meter composite depth (mcd). Technical gaps due to  
344 coring typically occur between individual core sections and were bridged down to 10.5 mcd by  
345 parallel and overlapping cores (Fig. 2). Beyond 10.5 mcd and until the basal depth of 14.4 mcd there  
346 are five intersections of which four could not be bridged due to lacking overlap. These gaps were  
347 assumed to be 3 cm wide based on the mean for similar technical gaps observed in the upper 10 m.

348 Initially, the scans of magnetic susceptibility ( $\chi$ ) were intended for core correlation. However, the  
349 variability of  $\chi$  was too low for this purpose (Figs. 3, S2). Moreover and above 9.7 mcd, LD17-A and  
350 LD17-B show mean values for  $\chi$  of  $-4.14$  SI and  $-3.98 \cdot 10^{-6}$  SI, respectively, i.e. in the field of  
351 diamagnetism. Only below 9.7 mcd  $\chi$  has positive mean values of  $7.51 \cdot 10^{-6}$  SI for LD17-A and  $15.43$   
352  $\cdot 10^{-6}$  SI for LD17-B, i.e. in the field of paramagnetism (Fig. S2). Thus, the record of Lagoa Dourada  
353 carries no ferromagnetic signal and  $\chi$  cannot be used for core correlation.

354 A test for total inorganic carbon (TIC) was carried out with 14 lithologically representative samples  
355 (Fig. 3). The detected values are very low and range between  $-1.99$  and  $2.49$  % TIC (mean:  $0.45$  % TIC)  
356 confirming our assumption that the sediment is basically free of carbonates like the catchment area.

357 Based on macroscopic as well as on microscopic sediment characterization and supported by bulk  
358 geochemistry and grainsize, the sediment record of Lagoa Dourada is subdivided into seven  
359 lithological units (lithozones A to G: LZ A-G) with six subzones (Figs. 2, 3). Basal LZ A1 (14.4-12.1 mcd)  
360 is a dark gray mud composed of up to 15 % BSi (opal of small planktonic central and pennate diatoms  
361 as well as few sponge spicules) but low amounts of TOC ( $\sim 3$  %) in a silt-rich matrix. The C/N ratio  
362 decreases from base (15) to top (10) of LZ A1, indicating increasing autochthonous OM supply. This  
363 development is interrupted by a gray layer of fine sand (LZ B1: 12.1-12.0 mcd) with almost no organic  
364 components. The following LZ C consists of laminated and diatomaceous dark gray mud (12.0-11.5  
365 mcd) with dominating pennate and very small (planktonic) diatoms. C/N ratios remain low (7-12) and

366 medium silt dominates the grainsize. Altogether, this evidences the development of a deeper lake  
367 system with peaking BSi (up to 30 %) and increasing TOC values (~5 %). LZ B2 (11.5-10.4 mcd) is a  
368 thick and structureless gray sand layer without organic components. With LZ A2 (10.4-10.0 mcd) the  
369 dark gray mud of LZ A1 returns. Compared to LZ A1, geochemical data of LZ A2 show markedly lower  
370 values for BSi (<3 %), while TOC increases to 7 % including more allochthonous organic material as  
371 indicated by rising C/N ratios. For the third intercalation of gray sand (LZ B3: 10.0-9.5 mcd) inorganic  
372 conditions recur with BSi and TOC documenting almost absence of OM.

373 With the advent of LZ D1 (9.5-8.9 mcd), sediments change markedly (Fig. 3). The bedded brown  
374 organic mud differs distinctly from all lithozones below. A color change to brownish hues indicates an  
375 increased importance of OM (mean TOC ~10 %) including plant macrofossils that explain the rise of  
376 C/N ratios to 32. Diatoms show comparable values (~3 % BSi) like in LZ A2. In addition to changes in  
377 color and OM, mean grainsize coarsens from dominance of medium silt in lithozones A and C to  
378 coarse silt in LZ D with frequent intercalations of fine sand. LZ D1 is followed by an intercalation of  
379 1.2 m of dark gray sand (LZ E1: 8.9-7.7 mcd) consisting mainly of fine sand without organic  
380 components. Following this sand layer, sediments continue with LZ D2 (7.7-6.7 mcd) and increasing  
381 TOC values (20 %). Diatoms remain at lower values (~3 % BSi) like before, while C/N ratios decrease  
382 to 20. After a second dark gray and fine sand horizon without organic components (LZ E2: 5.7-5.3  
383 mcd), bedded brown organic mud (LZ D3: 5.3-1.1 mcd) continues with increasing OM contents  
384 (maxima up to 30 % TOC) and slightly more diatoms (~5 % BSi), while C/N ratios decrease to 13.  
385 Throughout LZ D the mean grainsize remains in the coarse silt fraction, while organic productivity  
386 increases as documented by higher TOC and BSi values. At the beginning of LZ D3 the influence of  
387 allochthonous OM is still high (C/N >20) but decreases thereafter to <15. In LZ D3 amorphous OM is  
388 ubiquitous as well as pyrite, which often forms microscopically detectable framboids.

389 With LZ F (1.1-0.4 mcd) minerogenic sediments recur (Fig. 3). This pale brown to gray clay-rich mud  
390 displays a drop in lacustrine productivity to 2 % BSi and 13 % TOC (Fig. 3). Additionally, C/N ratios  
391 decline reaching low values of 11, thus indicating dominance of autochthonous OM. Grainsize  
392 changes to finest values of the record with a mean in the fine silt fraction and up to 33 % of clay.  
393 Finally, at the top of the record there is black, organic-rich and homogenous mud (LZ G: 0.4-0.2 mcd)  
394 with a higher water content and TOC values reaching 29 %, while the C/N ratio remains at ~10.  
395 Despite these productive conditions causing highly organic sediments, BSi remains <3 %.

#### 396 XRF scanning data: comparing litholog with clusterlog stratigraphies

397 The XRF scanner detected 20 elements (Al, Si, P, S, Cl, K, Ca, Ti, V, Cr, Mn, Fe, Ni, Cu, Zn, Br, Rb, Sr, Zr,  
398 Pb) with counts varying from 7 (Cl) to 21,607 (Fe) as well as coherent (coh) and incoherent (inc)  
399 radiation. Many of these elements have low signal-to-noise ratios and need to be excluded from  
400 further discussion. Five replicate XRF scans were carried out for 97 cm of organic sediment from  
401 LD17-B6 (LZs D2, E2 and D3) and 97 cm of minerogenic sediment from LD17-B12 (LZs A1, B1 and C).  
402 These records were used in correlation analyses to inform on the replicability of the signals. High  
403 correlations reveal a generally good reproducibility of elemental analyses (Tab. S1). Only elements  
404 with a high positive correlation ( $r > 0.8$ ) for at least one of the two scanned sediment sections are  
405 considered for further discussion (Tab. S1). Thus, ten elements (Si, S, K, Ca, Ti, Fe, Zn, Rb, Sr, Zr) as  
406 well as the inc/coh ratio are selected for principal component analysis (PCA) and cluster analysis.

407 The first two principal components (PCs) are representing 64.6 % of the explained total variance (Fig.  
408 4). Additional PC's explain <10 % and were not considered based on the elbow concept (Fig. S3). This  
409 first PC discriminates with 43.8 % of explained variance between organic (positive direction) and  
410 minerogenic sediment composition (negative direction). The second PC with 20.8 % of explained  
411 variance represents mainly the trends in grainsize variability with larger grainsizes related to the  
412 positive direction and smaller grainsizes to the negative direction. Hierarchical density-based spatial  
413 clustering of applications with noise (HDBSCAN) provides four distinct clusters (Fig. 4), which are  
414 transferred into a clusterlog to be compared with the litholog (Fig. 2). Although the number of

415 clusterlog units (4) is smaller than the number of litholog units (7), an overall agreement is evident.  
416 The discrepancies, i.e. merging of the LZs A with C, B with E as well as D with G, are related to XRF  
417 analyses capturing only heavier elements than Al. Thus, changes in organic sediment components  
418 consisting of lighter elements such as H, C and O are not detected.

419 Cluster 1 combines LZ B (light gray sand) with LZ E (dark gray sand), the latter being influenced by  
420 organic-rich pore water available from under- and overlying highly organic sediments of LZ D. The  
421 distinct link to Si and Zr relates these two sandy lithozones to weathering resistant minerals (quartz,  
422 zircon) of the Furnas Formation as their source rock. LZ A (dark gray mud) and LZ C (laminated and  
423 diatomaceous dark gray mud) together are related to cluster 2, which shows K, Ti and Rb as  
424 dominant siliciclastic elements. These elements likely originate from the Ponta Grossa Formation  
425 consisting of shales as potential source rocks.

426 Cluster 3 links to LZ F (reddish brown clay-rich mud) with Fe and Sr as dominant elements. As Fe is  
427 lacking in the Furnas Formation, these sediments derive from the iron-rich cement of the Vila Velha  
428 Sandstone. Moreover, PC loadings of Fe plot at the transition from minerogenic to organic  
429 components (Fig. 4), which indicates that Fe is not only bound to detrital silicates but also occurs as  
430 pyrite (FeS) and thus can as well be related to organic productivity. Sulphur is introduced to the  
431 sediment via lacustrine production of OM, which is deposited, decomposed and combined with  
432 dissolved Fe under anoxic (reducing) conditions typical for eutrophic lakes. Thus, there is a positive  
433 correlation between Fe and S for organic LZ D ( $r = 0.49$ ). However, the correlation for minerogenic  
434 LZs A and C is negative ( $r = -0.48$ ). This characteristic of Fe results in absence of any correlation  
435 between Fe and S if the entire record is considered ( $r = -0.20$ ).

436 In cluster 4, including LZs D (bedded brown organic mud) and G (black, organic-rich homogenous  
437 mud), the organic components S, Ca and the inc/coh ratio are combined. Despite this link to cluster  
438 4, Ca has a positive correlation with the siliciclastic elements K ( $r = 0.68$ ), Fe (0.50), Rb (0.68) and Sr  
439 (0.75) for LZs A1 and C. More dominantly than Fe, Ca is related to organic productivity, which might  
440 result from carbonaceous shells, which have been observed sporadically during coring. However,  
441 evidence for carbonate is lacking – TIC was not detected and XRD analysis is not promising because of  
442 very low calcite concentrations, as it was similarly documented for the highly organic sediment  
443 record from Laguna Azul (Zolitschka et al., 2019). Finally, the inc/coh ratio has a positive correlation  
444 ( $r = 0.88$ ) with TOC (Fig. S4) and thus provides a very high-resolution record of OM for the sediment  
445 record of Lagoa Dourada.

#### 446 XRF scanning data: stratigraphy of selected elements

447 High-resolution XRF core-scanning data support the lithological description. However, and due to  
448 their high spatial resolution of 2 mm, XRF records are more detailed and provide additional insights.  
449 All sand layers are reflected by distinct lows of the In inc/coh ratio as well as by pronounced peaks in  
450 Si (Fig. 5), both proxies clearly document inorganic quartz deposition. The high-resolution OM proxy  
451 (In inc/coh) displays a steady increase of organic productivity from the base of LZ A1 until the top of  
452 the record, if the sand layers and LZ F are taken out of consideration. However, a marked increase is  
453 observed at the onset of LZ D1, when dark gray mud changes to brown organic mud. This distinct  
454 sedimentological transition is even more pronounced for the S record, with low values prior to LZ D1  
455 and much higher values during LZ D1 (Fig. 5). After this major sedimentological transition S covaries  
456 with Fe, which is explained by diagenetic formation of pyrite (FeS). This mineral is formed under  
457 anoxic conditions and was determined by microscopic smear slide investigations as typical framboids.  
458 Such conditions also explain the higher degree of OM preservation during LZ D. During LZs A and C,  
459 Fe displays a decreasing trend and no covariation with S. Thus, we consider Fe as being related to a  
460 siliciclastic source for the older part of the record. This assumption is supported by the elements K  
461 and Ti. Both are siliciclastic and decrease as well during LZs A and C (Fig. 5).

462 The only marked change in the upper 5 m of the sediment record is related to the reddish-brown  
463 clay-rich mud of LZ F. During this lithozone, the organic parameters In inc/coh and S drop to distinctly  
464 lower values while Fe increases. We consider this as the result of an increased siliciclastic origin of Fe  
465 during LZ F, which is again supported by K and Ti values rising in parallel. For topmost LZ G, most  
466 elemental parameters seem to continue from where LZ D3 was interrupted by LZ F. Only the element  
467 K shows an unexpected increase during this lithozone peaking at higher values than during the entire  
468 LZ D.

#### 469 Grainsize statistics and sediment dynamics

470 Grainsize analysis documents two distinctly different populations (Fig. 6). Silty sand and fine to  
471 medium sand of LZs B and E are moderately well-sorted, unimodal and with one maximum in the fine  
472 sand fraction (Fig. S5). The other lithozones except LZ D3 consist of poorly sorted sandy silt or silt.  
473 They are characterized by bimodal grainsize distributions (Fig. S5) with maxima in the medium to  
474 coarse silt fractions and in the fine sand fraction (LZs A1 and F). Only LZ D3 displays a trimodal  
475 grainsize distribution with a broad maximum in the fine silt fraction and two narrow maxima in the  
476 fine and medium sand fractions (Fig. S5).

477 As there are no dunes or sand sheets in the catchment area to explain the moderately well-sorted  
478 sands of LZs B and E, we consider that this distinct unimodal grainsize distribution is inherited from  
479 sandstones of the Furnas Formation. During its relatively rapid flow through the karst hydrological  
480 system, the groundwater adds no additional grainsize fractions prior to deposition in Lagoa Dourada.  
481 Very different from the sand layers, the silt-sized sediment of LZs A, C and F probably originate from  
482 the shales of the Ponta Grossa Formation in the larger catchment area, which is drained via Rio  
483 Guabirola and enters the lake during flooding events where it settles out of suspension. As this  
484 suspension freight needs to be transported towards the lake against the slope of the outlet channel  
485 (Fig. 1), it is unlikely that the fine sand component observed by the secondary grainsize maximum  
486 rained out of suspension from river floods as well. Instead, we consider these sands as subordinated  
487 contribution from karstic springs, contributions which are coarser and more pronounced during LZs A  
488 and D compared to LZs C and F. Lithozone F has distinctly less fine sand, while there is a four-times  
489 higher contribution of clay.

490 Grainsize distributions provide insights into depositional processes at Lagoa Dourada. The two  
491 different sand horizons (LZs B and E) can only be differentiated by their color (Fig. 2), but have  
492 comparable unimodal grainsize distributions (Fig. S5) and an almost identical chemical composition  
493 (Figs. 4, 5). Based on the lack of OM and iron as well as on grainsize and chemical composition  
494 inherited from weathering-resistant minerals of the Furnas Formation, we consider these sands as  
495 event deposits related to flushing of the karst hydrological system. These sediments are added to the  
496 stratigraphic record in relatively short time intervals and thus are without temporal significance for  
497 the stratigraphic record. The other lithozones are dominated by silt-sized grainsize fractions, derived  
498 from suspension fallout, but also show a minor sandy component (bimodal grainsize distribution, Fig.  
499 S5) likely added by karstic springs. This sand component is least pronounced for LZs C and F. The  
500 highly organic LZ D shows a trimodal grainsize distribution (Fig. S5) with two maxima in the sand  
501 fraction, which is interpreted in terms of increasing importance of the karst system for the  
502 contribution of minerogenic components to the lake, while settling out of suspension was reduced.

#### 503 Age-depth model

504 All radiocarbon dates from terrestrial macrofossils are in stratigraphic order and their age-depth  
505 relationship is almost linear (Tab. 1, Fig. 7). Radiocarbon age determinations on bulk sediment also  
506 follow a linear age-depth trend with a cluster of three dates being too young and two dates being too  
507 old compared to the trend indicated by the other ten bulk dates. The two radiocarbon dates on bulk  
508 sediment above and below the terrestrial macrofossil at 7.3 mcd are too old by 5065 and 5235  
509 radiocarbon years, respectively (Tab. 1). The resulting average of 5150 years is used as an offset

510 applied to all bulk dates prior to calibration. Describing the uncertainty of this reservoir correction,  
511 an error of 100 years was added as contribution of old carbon to the sediment, which cannot be  
512 regarded as constant with time.

513 The resulting age-depth model suggests an age of 10,400 cal. BP for the basal sample (Fig. 7). The  
514 two aforementioned clusters of five bulk dates deviating from the general trend were not considered  
515 by the age model. It is noticeable that four out of five bulk dates deviating from the linear trend were  
516 obtained from sand sections. The radiocarbon date of the twiglet at 9.25 mcd was also compared to  
517 a neighboring bulk date resulting in an offset of 5145 years (Tab. 1), which confirms that the reservoir  
518 effect applied (5150 years) is applicable also for the older part of the record with much lower OM  
519 content.

520

## 521 **Interpretation**

522 Processes of sediment formation at Lagoa Dourada are differentiated into three modes according to  
523 their elemental composition and supported by cluster analysis (Figs. 3-5). The three involved  
524 depositional processes relate to (1) fluvial activities of Rio Guabiroba, (2) discharge through the karst  
525 hydrological system and (3) autochthonous lacustrine productivity. Contributions of all three  
526 processes vary through time. However, one of them can always be regarded as the leading  
527 depositional process. Prevalence of karstic runoff is considered for the five sand layers, i.e. cluster 1  
528 (Figs. 2, 4). As coarse-grained deposits they differ from the fine-grained silts related to seasonal  
529 flooding of the river. Therefore, they are regarded as short events and thus as stratigraphically  
530 insignificant. This is why these sand intercalations via karst hydrology are excluded from the  
531 discussion of past environmental conditions as well as from the selection of geochemical, elemental  
532 and sedimentological data plotted vs. time (Figs. 8-10). Based on these considerations, five different  
533 periods have been distinguished for this subtropical lake characterizing its Holocene environmental  
534 history.

535 (1) Early Holocene (10,400-7800 cal. BP) – dominance of fluvial sedimentation: This period is  
536 composed of LZs A1 and C and characterized by cluster 2 with increased values of Fe, K and Ti (Fig. 9)  
537 in a medium silt matrix. This type of sediment is introduced by suspension fallout during flooding of  
538 Rio Guabiroba. Moreover, the elemental composition excludes the Furnas Formation as the source  
539 for these deposits, because Fe and K are unknown from the sandstone of the Furnas Formation  
540 making river influence the only possible source. In terms of organic sediment components, the onset  
541 at 10,400 cal. BP reflects rather low values for TOC and BSi (Fig. 8). While TOC remains at such low  
542 levels throughout this period, diatom productivity (BSi) increases rapidly and reaches two distinct  
543 maxima at 8300 and 8000 cal. BP, both with microscopically detectable high numbers of planktonic  
544 diatoms. This increased diatom productivity might be fostered by relatively high amounts of K and Si  
545 together with other micronutrients essential for diatom growths introduced through fluvial  
546 discharge, while N remains rather low (Fig. 8) leaving non-siliceous algae at low numbers. In general,  
547 the lacustrine system of the Early Holocene is characterized by increasing nutrient levels, while the  
548 source of OM is dominantly lacustrine (C/N ratio: 10-15).

549 Rio Guabiroba flows on its flood plain with a very low gradient. This is indicated by the high degree of  
550 meandering along the river course (Fig. 1), which leads to the deposition of silt and sand in the river  
551 bed. During flooding, coarse silt and fine sand are deposited on the river banks forming a levee and  
552 finer grains cover the flood plain. Lagoa Dourada is situated on this flood plain and has a short-cut  
553 connecting river and lake. As flooding through this outflow channel occurs against the local gradient,  
554 flow velocity is expected to be low and only silt and clay can be transported and eventually deposited  
555 in the lake basin as suspension fallout. This process is supported by observations during coring, when  
556 low lake-water transparency due to high suspension loads occurred during a flood event changing to  
557 high lake-water transparency virtually hours after the flood event has ended.

558 Another aspect to be mentioned is the availability of fine-grained material for river transport and  
559 deposition. Initially such material needs to be eroded, but erosion only occurs if the soil is not well  
560 protected by vegetation. Moreover, the type of rainfall increases the susceptibility to erosional  
561 processes: episodic precipitation during a drier climate results in higher erosion rates compared to  
562 more evenly distributed precipitation during a wetter climate. This would exclude forest as  
563 vegetation type for the Early Holocene as it protects from soil erosion. Thus, decreasing silt  
564 deposition during the subsequent early Middle Holocene transitional period is explained by  
565 woodland expansion as the consequence of higher rainfall reducing soil erosional processes. Another  
566 possible explanation could be that levees have been created in the course of several millennia  
567 protecting the flood plain more efficiently from flooding.

568 The final centuries of the Early Holocene (8300-7800 cal. BP) are characterized by an all-time  
569 maximum in planktonic diatom development (Fig. 8), a marked decrease in Ti as well as a distinct  
570 increase in K (Fig. 9). Together, this could be explained by increased precipitation, which would  
571 correspond to less soil erosion due to a denser vegetation cover (Ti), a higher degree of chemical  
572 weathering with related leaching of K and a deeper lake with more nutrients beneficial for planktonic  
573 diatom development (Fig. 9). This wetter period may represent the 8.2 ka event, which is  
574 characterized – according to model simulations – by more rainfall in S Brazil as a result of North  
575 Atlantic cooling and monsoon enhancement across Brazil (Morrill et al., 2013).

576 (2) Early Middle Holocene transition (7800-6200 cal. BP) – from dominance of fluvial influence to  
577 autochthonous lacustrine deposition: This combination of LZs A2 and D1 is a two-partite transitional  
578 period belonging to clusters 2 and 4. On the one hand, BSi drops from 20 to 3 % right at the  
579 beginning of this period and remains constantly low further on. On the other hand, TOC triples to  
580 values up to 15 %. This development goes along with an increase of the C/N ratio from 12 to 30, a  
581 change starting with a delay of 400 years, which indicates a higher influence of allochthonous OM  
582 interpreted as a decrease in water depth with less lacustrine and more catchment derived OM. This  
583 parallels an increase in mean grainsize from 20  $\mu\text{m}$  (middle silt) to 70  $\mu\text{m}$  (fine sand). C/N and  
584 grainsize remain at their high levels until the end of the early Middle Holocene at 6200 cal. BP. A  
585 component related to OM that additionally comes into play during the latter part of this period is S  
586 (Fig. 9). This element is low during the first part of this transition and increases markedly after 7400  
587 cal. BP – a change that goes along with an increase in Fe. Formation of pyrite explains this process  
588 pointing to anoxic conditions at the lake floor and being responsible for the color change to darker  
589 hues with the onset of LZ D1. Finally, elements of the minerogenic sediment component relating to  
590 the river catchment area as source (K, Ti) loose importance towards the end of this transitional  
591 period (Fig. 9).

592 There are two possible options explaining the transition from silt-dominated sediments poor in OM  
593 to an increasing sand-dominance with more allochthonous OM. The general process behind this  
594 development is less influence of river flooding. Simultaneously, increasing influence of organic  
595 lacustrine productivity and/or runoff from the immediate catchment area of Lagoa Dourada with  
596 influx of allochthonous OM such as leaves and twigs is reflected by higher C/N ratios. Buildup of  
597 levees preventing the floodplain from flooding could be regarded as an explanation. However, as the  
598 outflow channel from the lake always keeps an opening in the levee, this option seems unlikely.  
599 Instead, it is more likely that higher and more evenly distributed precipitation increased the density  
600 of vegetation, which on the one hand protects soils in the wider catchment area of Rio Guabiroba  
601 from erosion and thus reduces availability and river transport of fine-grained minerogenic matter. On  
602 the other hand, less suspension transport of the river frees fluvial energy increasing incision rates  
603 into the river bed and reducing the likelihood of flooding. As the second mechanism can be explained  
604 favorably by increased rainfall, we assume this process to be the most likely case explaining the  
605 change in depositional processes.

606 More precipitation is also regarded as the reason for (1) higher activity of the karst hydrological  
607 system responsible for introducing sand into the lake; (2) intensified chemical weathering and thus  
608 increased pedogenesis in combination with denser vegetation making available more nutrients such  
609 as N and P (cf., Fig. 3 for N). Additionally, the decrease in diatom abundance suggests other algae,  
610 such as blue-green algae (cyanobacteria), as being responsible for a fueled lacustrine productivity  
611 leading to anoxia at the lake bottom with formation of pyrite; and (3) an increased density of  
612 vegetation, which explains the higher contribution of allochthonous and lignin-rich OM responsible  
613 for increasing C/N ratios (Fig. 8). The underlying change from a drier to a wetter landscape with  
614 adapting vegetation might be considered as the reason for this transition indicated by highest C/N  
615 ratios and sand influx. It is interesting to note that this transitional period is framed by two (LZs B2  
616 and E1) and includes a third (LZ B3) out of five sand horizons, which make up almost 87 % of the  
617 thickness of all sand layers. This also confirms a higher activity of the karst hydrological system in the  
618 catchment area.

619 (3) Late Middle Holocene (6200-3800 cal. BP) – stabilization of lacustrine deposition: During the late  
620 Middle Holocene (LZ D2) the ecosystem stabilized with increasingly organic sediment deposition.  
621 Although BSi remains at its low level, TOC continues to rise to 20 % until 4600 cal. BP, when a distinct  
622 drop to 10 % occurs until 3800 cal. BP (Fig. 8). The only other parameter marking this change is  
623 grainsize, which coarsens towards a mean of >100  $\mu\text{m}$ . Thus, the drop in TOC likely is a result of  
624 dilution by additional quartz grains. However, the C/N ratio is decreasing (Fig. 8), which excludes  
625 intensified surface runoff and suggests a stable catchment system with increased influx of sand via  
626 karstic springs. This is supported by continuing high levels of S indicating anoxia as the result of  
627 increased organic lacustrine productivity probably dominated by blue-green algae.  
628 Altogether, the lacustrine system further stabilized during this period as well as the catchment area,  
629 from where less terrestrial organic remains enter the lake and thus cause the C/N ratio to decrease.  
630 However, between 4600 and 3800 cal. BP and thus prior to the onset of the Late Holocene, an  
631 increased activity of the karst hydrological system indicates wetter environmental conditions not  
632 only causing an increase in grain size but also the formation of the youngest sand layer (LZ E2) at this  
633 transitional period.

634 (4) Late Holocene (3800-150 cal. BP) – mature lacustrine deposition: The Late Holocene lake system  
635 matures in the course of LZ D3. OM steadily increases to a maximum of >25 % TOC and also BSi  
636 doubles to 5 %. At the same time, the C/N ratio decreases indicating a more prominent contribution  
637 of autochthonous lacustrine OM. This is supported by S remaining at the same high level as during  
638 the Middle Holocene and thus documents the presence of anoxia at the lake bottom. Grainsize  
639 diminishes from a mean of 50 to 30  $\mu\text{m}$  as well as siliciclastic elements (K, Ti) decrease, indicating a  
640 minimum of minerogenic components. Altogether, the lake develops towards more eutrophic  
641 conditions with two TOC maxima at 1750 and 1000 cal. BP.

642 The ending of LZ D3 is characterized by distinctly dropping values for Ti and K, which is best explained  
643 by denser vegetation inhibiting soil erosion. This interpretation argues in favor of higher precipitation  
644 as the responsible factor, i.e. a strengthening of the SAMS, comparable to the observation made for  
645 the 8.2 and 4.2 ka events. Due to more humid conditions with distinctly reduced export of erosion-  
646 related elements Ti and K (lowest value of the entire record for Ti), these four centuries are related  
647 to the LIA. However, the timing as determined by the radiocarbon-based age-depth model is 1000-  
648 600 cal. BP (AD 950-1350; Fig. 10) and would be too old if compared to other available dates for the  
649 LIA in the Southern Hemisphere: 600-150 cal. BP or AD 1350-1800 (e.g., Bernal et al., 2016b). As the  
650 onset of the LIA is very distinct, we use this transition to adjust our chronology with the date of AD  
651 1350 for the beginning of the LIA (Fig. S6). The radiocarbon-based age-depth model (Fig. 7) provides  
652 an older age because the youngest  $^{14}\text{C}$  age is 850 cal. BP (AD 1100). As the lithology is quite variable  
653 during the last millennium, a higher degree of variability has to be expected for the sedimentation  
654 rate, which is modelled as linear due to the lack of data points (Tab. 1, Fig. 7).

655 (5) Human impact – returning dominance of fluvial sedimentation during the last two centuries:  
656 Drastic sedimentological changes occur after the preceding mature period within LZs F and G. Not  
657 only TOC, BSi, C/N ratio and grainsize decrease markedly in LZ F (Fig. 8), also all elemental data (Fig.  
658 9) respond accordingly: S and Si drop to lower values while Fe, K and Ti increase. S covaries with all  
659 organic productivity indicating proxies, which either points to a drop in organic productivity or to  
660 dilution by minerogenic matter. The latter seems to be the more likely explanation here because Fe is  
661 no longer correlating with S but with K and Ti instead. This indicates an increased presence of  
662 siliciclastic matter, which is supported by a change in color and higher K and Ti levels. The  
663 simultaneous drop in Si as well as the presence of Fe suggest that during this period the lake again  
664 received suspended sediment loads from Rio Guabirola. The fine silt fraction observed has a mean  
665 grainsize of 6  $\mu\text{m}$  with highest contributions of clay (up to 33 %) and elevated Fe and K contents.  
666 These are not components of the Furnas sandstone but were produced by chemical weathering and  
667 pedogenesis of shales from the Ponta Grossa Formation.

668 If this sediment is the result of re-activated flooding of the river (cluster 3 of Fig. 4) then the question  
669 arises, which processes caused these deposits and shape them so markedly different from Early  
670 Holocene suspension load (cluster 2 of Fig. 4). The most convincing explanation includes human  
671 activity related to land-use change. Since the Middle Holocene, the vegetation became denser during  
672 wetter environmental conditions. These climatic conditions intensified chemical weathering and  
673 pedogenesis and thus altered the soils causing enrichment in Fe, depletion in K and formation of the  
674 clay mineral kaolinite. These soils were stabilized by vegetation until European farmers claimed the  
675 land. While vegetation protects soils from erosion even under high rainfall conditions, land clearance  
676 immediately triggered erosional processes (cf., Zolitschka, 1998) often with the help of fire. As the  
677 soil-protecting canopy and stabilizing root systems were removed, less water is stored in vegetation  
678 and in soil OM increasing surface runoff and causing soil erosion. Relocated downslope, the river  
679 picks up the eroded material and transports it towards Lagoa Dourada. This high sediment freight of  
680 Rio Guabirola gave rise to a high amount of deposition in the river bed, thus decreasing its cross  
681 section and at the same time increasing the probability of flooding, which is regarded as the reason  
682 for deposition of LZ F.

683 However, this plausible interpretation of LZ F contradicts with the radiocarbon-based age-depth  
684 model suggesting 600 cal. BP (AD 1350) for the onset of human activities. This date opposes historical  
685 data of first European settlements in the region around Ponta Grossa at ca. AD 1800 (Freitas, 2011)  
686 with still marginal influences on the landscape, which was initially restricted to cattle breeding. Only  
687 decades later, land-use change accelerated around 1850 (Freitas, 2011). Altogether, this challenges  
688 the age-depth model for the last millennium with only one radiocarbon date at 850 cal. BP (Tab. 1,  
689 Fig. 7). We, therefore, add the historical date of AD 1800 (150 cal. BP) for the onset of agricultural  
690 activities in the hydrological catchment (Fig. S6).

691 Another explanation of clastic LZ F needs to be discussed assuming the age-depth model is correct  
692 (Fig. 7). For the time from 600-150 cal. BP (AD 1350-1800) natural climatic variability, such as the LIA,  
693 might be considered as a reason. Only few paleorecords provide evidences of the LIA for S Brazil.  
694 However, this is most likely a matter of temporal resolution being less adequate for detecting this  
695 rather short climatic fluctuation (cf., Bernal et al., 2016b). However, assuming the LIA as the reason  
696 for LZ F, causative processes are not supported by the sediment record of Lagoa Dourada. The impact  
697 of the LIA on climatic conditions for S Brazil is increased precipitation (Bernal et al., 2016b; Novello et  
698 al., 2021). Consequently, this is leading to denser vegetation with less soil erosion, a process  
699 described for the centuries immediately prior to LZ F. Thus, we refuse the option of considering the  
700 LIA as responsible for increased minerogenic deposition during LZ F and find further support for a  
701 necessary modification of our chronology for the last millennium (cf., Fig. S6).

702 This interpretation in combination with the modified age-depth model is supported by topmost  
703 lithozone (LZ G), which is characterized by a return to highly organic deposits (Fig. 8) around AD 1950



704 (0 cal. BP). This corresponds to the establishment of the Vila Velha State Park in AD 1953. Thus, we  
705 can add another “historical” date to modify our chronology of the last millennium (Fig. S6). In  
706 combination with plantations of pine and eucalypt during the following decade, soil erosion was  
707 reduced. A return to highly organic sediments comparable to those prior to AD 800 was the result,  
708 except for two elements: N (Fig. 3) and K (Figs. 5, 9). Both elements increase considerably towards  
709 the top of the record, a process explained by the extensive use of fertilizers in the catchment area  
710 since the 1950ies.

711 (6) Refining the chronology: Altogether, we add three ages to our record to refine the radiocarbon-  
712 based chronology of the last millennium (Fig. S6):

- 713 ○ The onset of LZ G is linked to the establishment of the Vila Velha State Park in AD 1953 with a  
714 return to highly organic sediments caused by less soil erosion in the now (partly) protected  
715 catchment area in combination with intensified use of fertilizers causing eutrophication since  
716 the 1950ies (0 cal. BP);
- 717 ○ The onset of human influence with related agricultural activities and land-use changes  
718 causing high rates of soil erosion starting around AD 1800 ±50 (150 ±50 cal. BP) and
- 719 ○ The onset of the LIA with higher precipitation and denser vegetation leading to less leaching  
720 of elements like K and Ti, which is anticipated for AD 1350 (600 cal. BP).

721

## 722 **Discussion**

723 Chronological considerations: Evidences in support of an Early Holocene basal age of the recovered  
724 sediments come from various sources. Although the oldest uncalibrated radiocarbon ages date the  
725 sediment core LD91 to 11,170 ±110 BP (Melo et al., 2003; Moro et al., 2004) and LD17-ID23 to 13,850  
726 ±70 BP and 14,660 ±80 cal. BP (Tab. 1), these ages document influences of reservoir effects and are  
727 not providing a Lateglacial age for the basal sediments of Lagoa Dourada. This is confirmed by pollen  
728 and speleothem data. Palynological investigations at Serra dos Orgaos (22.5 °S) describe a warm and  
729 wet YD chronozone, which extends from 12,700-11,600 cal. BP (Behling and Safford, 2010). Similar  
730 climatic conditions are reconstructed with pollen from Serra do Tabuleiro at 28 °S (Behling and  
731 Oliveira, 2017). Additionally, the reconstruction of precipitation using stable isotopes of a  
732 speleothem from Botuverá Cave at 27 °S (Cruz et al., 2005) also characterizes the YD as wet  
733 comparable to the Late Holocene (Fig. 10A). There is no evidence for such a warm and wet period  
734 with forest expansion at the base of our record (Piraquive Bermúdez, 2020). Thus, we have further  
735 evidence that the obtained Lateglacial ages really are artefacts and the record from Lagoa Dourada  
736 starts with the Early Holocene.

737 Information about the age of the uppermost meter of sediment is deduced with links to the regional  
738 historic development. The pollen diagram of Cambara do Sul (29 °S) has a high sample resolution for  
739 the last centuries and indicates human activities. At this site European land use started after AD  
740 1780, first with cattle breeding followed by logging. Since AD 1820, settlements were established  
741 with accompanying agriculture (Behling et al., 2004). Furthermore, historic evidence for the  
742 introduction of neophytes (eucalypt and pine trees) to S Brazil dates back to AD 1904, when timber  
743 barons established first tests with these fast-growing tree species (Ayling and Martins, 1981).  
744 However, commercial eucalypt plantations near Lagoa Dourada did not occur before the mid-1960ies  
745 (Ayling and Martins, 1981). They are reported for Vila Velha State Park for AD 1964 (Government of  
746 the State of Paraná). Thus, we are confident that LZ G covers only the last ~70 years. The reason for  
747 the discrepancy between historical data and the radiocarbon-based age-depth model is the lack of  
748 <sup>14</sup>C ages for the last millennium, where distinct changes in sedimentation rate have implications for  
749 sedimentation rates (Fig. S6).

750 Comparison with previously published data from Lagoa Dourada: Sediments from Lagoa Dourada  
751 (LD91) have been cored for the first time more than 30 years ago (Melo et al., 2003; Moro et al.,  
752 2004). However, this record is severely hampered by (1) very general sediment descriptions differing  
753 between Melo et al. (2003) and Moro et al. (2004); (2) many data are only available with low spatial  
754 resolution, i.e. one or two analyses per meter; and (3) the chronology is based on two radiocarbon  
755 dates only providing ages of  $11,170 \pm 110$  BP and  $8720 \pm 150$  BP from 11.9 m and 10.6 m of LD91,  
756 respectively. With these dates, a Lateglacial age has been proposed for the basal sediments at 12.2  
757 m. As a result of our study, these ages should be considered cautiously and not without considering a  
758 reservoir correction. Despite of these limitations, Melo et al. (2003) provide mineralogical data based  
759 on XRD analyses, which document the presence of quartz, kaolinite, illite, pyrite and gypsum. The  
760 latter is certainly an artefact and produced after core splitting when pyrite (FeS) oxidized and  
761 recrystallized as gypsum (CaSO<sub>4</sub>). As total carbon percentages of this old record are erroneously low  
762 (<0.83 %), the presence of pyrite together with gypsum is interpreted as an indicator of dry (semi-  
763 arid) climate conditions prior to 8720 BP and as well for a period between 5000 and 3000 BP (Melo et  
764 al., 2003). Furthermore, it is argued that the sand horizons are related to semi-arid conditions, when  
765 river runoff and thus flooding events did not occur while karstic springs provided water with quartz  
766 grains. While our study does not support these assumptions, the detection of a planktonic diatom  
767 maximum at 11.8 m by Moro et al. (2004) agrees with LZ C with its high BSi values and the  
768 microscopic detection of planktonic diatoms. Moreover, Moro et al. (2004) confirm the high  
769 concentration of K for a depth of 20 cm, which they relate to NPK fertilizers applied in the catchment  
770 area, results that also agree with our study.

771 Comparison with pollen data from S and SE Brazil: Most paleoenvironmental data from S and SE  
772 Brazil is from palynological investigations. Here we compare our investigation with pollen records  
773 spanning a latitudinal range from 18 to 28 °S.

774 The pollen record from Serra do Tabuleiro (28 °S) provides a nicely dated and densely analyzed Early  
775 Holocene record (Behling and Oliveira, 2017). After the warm and wet second half of the YD, Campos  
776 vegetation (grassland) with a warm and dry climate dominated the Early Holocene until 8000 cal. BP.  
777 Compiling eleven pollen records covering the latitudes between 15 and 35 °S, Ledru et al. (1998)  
778 document warm and dry Early Holocene climatic conditions for the time period 11,400-7700 cal. BP.  
779 In a comparable synthesis, Behling (2002) uses 14 pollen records between 18 and 28 °S and suggests  
780 ~6300 cal. BP as the end of warm and dry Early Holocene conditions. This data supports our  
781 interpretation of environmental conditions at Lagoa Dourada, where grassland vegetation under dry  
782 and warm climate conditions is proposed to explain erosion of fine-grained material in the catchment  
783 area via slope-wash (no or much less trees to protect against soil erosion), river transport and  
784 flooding until 7800 cal. BP (Fig. 8). This is also supported by data from NE Brazil, where the Middle  
785 Holocene shift from forest to grassland vegetation (Caatinga), i.e. from wet to dry conditions, caused  
786 an increase in soil-erosion rates due to less dense vegetation exposing soils to erosion during  
787 precipitation events (Jaqueto et al., 2016; Utida et al., 2020). In SE Brazil, this process not only caused  
788 intense colluvial deposition but also the formation of high fluvial terraces in the drainage systems of  
789 rivers dated to 11,400-9500 cal. BP (Suguoio et al., 1989).

790 After a warm and dry onset of the Holocene, precipitation started to increase, causing a change from  
791 Campos vegetation to the development of forest at Serra do Tabuleiro (Behling and Oliveira, 2017).  
792 Increased moisture advection from the Amazon Basin with a weakening of polar advection results in  
793 an expansion of forests in S Brazil dated to 7700-4390 cal. BP (Ledru et al., 1998). This process is not  
794 consistent in timing across S and SE Brazil (cf., Behling, 2002), a fact that may be due to the large  
795 latitudinal extension (1300 km) of available data, differences in elevation between coastal plains and  
796 the mountainous hinterland, chronological uncertainties and also to a time-transgressive spatial  
797 evolution or gradual shift of climatic conditions (Rodrigues et al., 2016). Higher rainfall with the  
798 expansion of forests is noted by other pollen records for a time period from 8900 until 5700 cal. BP  
799 (Behling, 1995, 2003; Behling and Oliveira, 2017; Behling and Safford, 2010; Enters et al., 2010;

800 Rodrigues-Filho et al., 2002). This change from grassland to forest reduced hillslope denudation to a  
801 minimum and increased chemical weathering and pedogenesis with leaching of nutrients as  
802 documented by increased lacustrine productivity, e.g. at Lago Aleixo (Enters et al., 2010). This also  
803 transformed lacustrine sedimentological processes at Lagoa Dourada and at Lago Silvana at 19,5 °S  
804 from silt-rich suspension fallout to Fe-rich organic sediments (Rodrigues-Filho et al., 2002).

805 Organic deposition continued until the last millennium when a few sites document a climatic  
806 fluctuation related to the LIA with warm and wetter climatic conditions. These have been detected  
807 for AD 1520-1780 at Cambara do Sul (Behling et al., 2004) and since AD 1390 at Lagoa Nova (Behling,  
808 2003). For Lagoa Dourada less siliciclastic matter (K and Ti; Fig. 9) is detected and possibly related to  
809 the LIA dated to AD 1350-1800 according to the modified chronology (Fig. S6).

810 Finally, human activities changed the ecosystems. Since the late 18<sup>th</sup> century, European settlers  
811 started to use the area for farming (Behling and Oliveira, 2017; Portes et al., 2018). Agricultural  
812 activities (logging, cattle breeding, tillage) gave rise to increased soil erosion, as documented for  
813 Lagoa Dourada and less prominent for Lago Aleixo (Enters et al., 2010). In both cases, organic  
814 sediments were replaced by minerogenic sediments.

815 Comparison with other paleoclimate data: Speleothems currently provide the best dated climatic  
816 parameters for the reconstruction of precipitation in NE and SE Brazil (Baker and Fritz, 2015). In a  
817 distance of only 240 km SSE from Lagoa Dourada, speleothems from Caverna Botuverá (27 °S)  
818 provide high-resolution stable isotope data with a precise U/Th-based chronology dating back to 116  
819 ka (Cruz et al., 2005). The obtained oxygen-isotope records (Fig. 10A, B) vary with the source of  
820 precipitation and thus are interpreted as proxies for atmospheric circulation and convective  
821 intensity, both closely related to the SAMS controlling hydroclimatic conditions. Summer convection  
822 over the Amazon Basin and associated monsoonal precipitation in S Brazil has a more negative  
823 oxygen isotope signature compared to winter rain related to incursions of mid-latitude storm  
824 tracks from the Atlantic Ocean (Cruz et al., 2005). These conditions are nicely summarized by Wang  
825 et al. (2007): “Low (high) Botuverá speleothem  $\delta^{18}\text{O}$  indicates intensified (weakened) SAMS activity,  
826 more (less) Amazon moisture contribution and higher (lower) rainfall in S Brazil.” Thus, the isotopic  
827 record from Caverna Botuverá is linked to variability in precipitation caused by insolation-controlled  
828 fluctuations of the SAMS and provides one of the most robust climate reconstructions for South  
829 America. While the early studies of Caverna Botuverá focus on orbital to millennial timescales (Cruz  
830 et al., 2005; Wang et al., 2007), follow-up investigations obtained a much higher temporal resolution  
831 for the Holocene detecting decadal to centennial climatic variability (Bernal et al., 2016b; Novello et  
832 al., 2021), data which also are used for inter-hemispheric correlation of climate modes (Deininger et  
833 al., 2020). The high-resolution  $\delta^{18}\text{O}$  data are supported by even higher resolving trace-element data  
834 (Mg, Ca, Sr, Ba). Especially the Sr/Ca ratio correlates highly with  $\delta^{18}\text{O}$  (Fig. 10B, C) and is applied as a  
835 proxy that characterizes SAMS intensity and detects the effect of Holocene climate anomalies on  
836 regional hydroclimatic conditions while closely following summer insolation at 30 °S (Bernal et al.,  
837 2016b). These data document a suppressed SAMS intensity during the Early Holocene and an  
838 increase starting around 7000 cal. BP. Due to the well-dated and high-resolution record, also  
839 centennial climatic events of the Holocene have been detected: the 8.2 ka event and the LIA for the  
840 time interval AD 1400-1850 (Bernal et al., 2016b) – both characterized by wetter hydroclimatic  
841 conditions. A wet LIA (AD 1600-1850) with stronger SAMS is also documented by a compilation of  
842 speleothem  $\delta^{13}\text{C}$  data from 25 caves in tropical and subtropical South America (Novello et al., 2021).

843 In addition to the pronounced signals related to the 8.2 ka event and to the LIA, another century-long  
844 climatic fluctuation is described for a sediment core from Lagoa Salgada (21 °S and ~1000 km NE of  
845 Lagoa Dourada in Rio de Janeiro State) and linked to the 4.2 ka event (Soares Cruz et al., 2019). This  
846 climatic fluctuation is considered as a time of exceptional climatic anomalies worldwide, although its  
847 cause is still under discussion (Bradley and Bakke, 2019; Giesche et al., 2019; Kathayat et al., 2018;  
848 Scuderi et al., 2019). At Lagoa Salgada, a tripartite period of wetter climate conditions with a short

849 central dry period is documented by geochemical, sedimentological and pollen investigations for the  
850 period 4200-3800 cal. BP (Soares Cruz et al., 2019). This climatic fluctuation corresponds to lower  
851 Mg/Ca and Sr/Ca ratios of the speleothem record from Caverna Botuverá supporting a generally  
852 wetter climate with a short central and dry period (Bernal et al., 2016b), while the high-resolution  
853 marine sediment record from Cariaco Basin (Venezuela) provides evidence for an overall drier  
854 climate with a short central wet section north of the equator (Hughen et al., 1996). The dry  
855 conditions at Cariaco Basin are considered to be the result of a southward shift of the ITCZ, which  
856 consequently can be regarded as the reason for wetter conditions in SE Brazil resulting from an  
857 intensification of the SAMS (Hughen et al., 1996; Soares Cruz et al., 2019).

858 All this hydroclimatic data agrees with our interpretation of the high-resolution record from Lagoa  
859 Dourada. The speleothem record underlines the observed environmental changes and provides the  
860 best possible precipitation signal solidifying the reconstructed surface processes that lead to the  
861 formation of the studied sediment sequence (Fig. 10D, E). The 8.2 ka event is characterized at Lagoa  
862 Dourada by increased BSi related to a maximum in planktonic diatom development (Fig. 8), a marked  
863 decrease in Ti and an increase in K (Figs. 9, 10D, E). These two centuries match with increased  
864 precipitation, which corresponds to less soil erosion due to denser vegetation (decrease in Ti), a  
865 higher degree of chemical weathering with related leaching of K with not yet enough vegetation to  
866 retain all the released K in organic tissue (increase of K) and a deeper lake with enough nutrients  
867 beneficial for the development of planktonic diatoms (Fig. 8). Despite of the diatom blooms,  
868 lacustrine productivity remains at a low level with overall minerogenic sediments being deposited.

869 The 4.2 ka event occurs at Lagoa Dourada from 4400-3800 cal. BP and in a tree-rich landscape with  
870 denser vegetation (Fig. 10). Thus, the increase in rainfall does not cause a decrease in soil erosion like  
871 during the 8.2 ka event as vegetation is already protecting the soils. Consequently, Ti shows no  
872 response to this event. The element K, however, has lower values because denser vegetation more  
873 efficiently inhibits K from being leached (Fig. 10). Less nutrient transfer from the catchment area to  
874 the lake might be one of the reasons for the contemporaneous drop in sediment organic matter at  
875 Lagoa Dourada (Fig. 8). Another explanation for this to occur is dilution by minerogenic matter, which  
876 is documented by a coarser mean grain size (Fig. 8), possibly linked to intensification of the karst  
877 hydrological system during this wet period. Also, diatoms play no major role anymore. They are  
878 subordinated since the end of the 8.2 ka event, when sediment composition switched from  
879 minerogenic to organogenic, probably due to generally higher influx of nutrients like N and P during  
880 the Middle and Late Holocene. Under such conditions, blue-green algae often outcompete diatoms,  
881 which explains why siliceous algae did not recover to the high values of the Early Holocene.

882 The responses of the lacustrine system of Lagoa Dourada to the climatic deterioration of the LIA is  
883 more or less comparable to the 4.2 ka event. However, on the one hand TOC decreases and mean  
884 grain size increases only slightly, while on the other hand BSi has a minor maximum (Fig. 8).  
885 Tentatively, this is interpreted as resulting from wetter conditions compared to the 4.2 ka event with  
886 distinctly denser vegetation, which reduces soil erosion (drop in Ti) and leaching of nutrients (drop in  
887 K) in the catchment area (Fig. 10). In consequence, this might have caused a less nutrient-rich lake  
888 leading to the observed increase in diatoms.

889 Comparison with archaeological data: Human population dynamics are in the focus of archaeological  
890 investigations of South America. Using radiocarbon dates of archaeological sites from the entire  
891 continent, a spatiotemporal pattern of human population growth has been reconstructed (Goldberg  
892 et al., 2016; Riris and Arroyo-Kalin, 2019). Aside from cultural and technological developments,  
893 climate change is considered as an additional factor modifying population dynamics. In this respect, it  
894 is interesting to note that one center of population growth is the area of the S Brazilian coast for the  
895 time interval 6000-4000 cal. BP (Goldberg et al., 2016). This period corresponds to the late Middle  
896 Holocene stabilization period of the record from Lagoa Dourada (Fig. 8) with forests being well  
897 established providing stable food resources. In another study, climate is considered as a driver of

898 cultural change and depopulation is attested for the Middle Holocene (8200-4200 cal. BP) with  
899 overall dominance of more arid climate conditions in South America (Riris and Arroyo-Kalin, 2019).  
900 However, their regionalization model provides a different picture for what is called the “Southern  
901 Cone”, i.e. the subtropical and temperate southern part of the continent, with significantly higher  
902 population between 7500 and 4500 cal. BP compared to other regions of South America (Riris and  
903 Arroyo-Kalin, 2019). Again, this can be related to the stabilization period of the late Middle Holocene  
904 at Lagoa Dourada. Altogether, climate is not only the driver for biological and geomorphological  
905 systems but also responsible for demographic change of human populations. To better understand  
906 this complex system Earth, it is pertinent to provide more high-resolution and well-dated information  
907 for environmental reconstruction from natural archives with a larger regional coverage in South  
908 America.

909

## 910 **Conclusions**

911 Thirty years after first investigations of sediment from Lagoa Dourada (S Brazil), our re-visit of this  
912 site provides a wealth of information shedding new light on environmental responses triggered by  
913 dominating climatic control mechanisms, which are related to intensity variations of the South  
914 American Monsoon System (SAMS). We recovered two overlapping sediment profiles with a basal  
915 depth of 14.4 mcd. Time control is obtained by applying sophisticated age-depth modelling after  
916 combining AMS radiocarbon dates on terrestrial macrofossils with reservoir-corrected ages of bulk  
917 organic matter. Based on this chronology, XRF core-scanning data together with geochemical and  
918 sedimentological studies provide high-resolution insights into responses of lacustrine and  
919 geomorphological systems to climatic variability and anthropogenic impacts. Altogether, the  
920 sediment record of Lagoa Dourada constitutes a powerful tool for investigating a detailed regional  
921 hydroclimatic history of the Holocene with unequivocal linkages to other regional and high-  
922 resolution studies, namely the speleothem records from Caverna Botuverá (Bernal et al., 2016b;  
923 Novello et al., 2021).

924 Based on statistical analyses of the high-resolution dataset from Lagoa Dourada, four different  
925 sediment sources were characterized geochemically and relate to lacustrine organic productivity,  
926 underground karst runoff, river flooding and cultural soil erosion. Thus, our comprehensive and well-  
927 dated multiproxy dataset provides a handle on process-related developments in the lake and its  
928 catchment area and allows insights into physical landscape changes as well as into geomorphological  
929 and lacustrine processes – all reflecting environmental responses to hydroclimatic variability during  
930 the Holocene and to human activities during the last two centuries. As such, this new record from  
931 Lagoa Dourada fills a knowledge gap with regard to hydroclimatic variability and its impact on  
932 environmental systems for S Brazil and beyond. Moreover, these sediments provide an essential  
933 contribution to understand how precipitation changes influenced the resilience of ecosystems and  
934 their responses to global climate change, which is important background information to better  
935 constrain model projections of future precipitation and their impacts on environmental change.

936 Our high-resolution data documents dominating flooding through Rio Guabiroba with suspension  
937 fallout of minerogenic particles transferred to the lake via fluvial activity during the Early Holocene.  
938 Between 7800 and 6200 cal. BP, a transition to highly organic lacustrine deposits is observed, when  
939 fluvial influences were replaced by increasingly organic lacustrine deposition. This is due to  
940 decreasing availability of minerogenic particles from hillslope denudation and river transport as a  
941 result of intensified pedogenesis under developing forests. Furthermore, this transition period is  
942 characterized by sand horizons, which link to more runoff through the karst hydrological system – a  
943 process less well understood but also linked to increased precipitation. Once established,  
944 autochthonous lacustrine processes dominate sediment formation for the remaining Holocene,  
945 except for the topmost centuries. Based on a modified chronology for the last millennium, European

946 settlers caused severe soil erosion as a result of land-use change between AD 1800 and 1950. For the  
947 youngest ca. 70 years, organic deposition reconvenes with evidences of increased eutrophication  
948 documented by high values for nitrogen and potassium acting as nutrients for lake biota.

949 The climatic development from a warm and dry Early Holocene to a warm and wet Middle and Late  
950 Holocene is in response to a strengthening of the SAMS. In addition to this general trend, the  
951 sediment record from Lagoa Dourada documents three of the two most prominent Holocene climatic  
952 events: the 8.2 ka event, the 4.2 ka event and the Little Ice Age. For Lagoa Dourada, these reflect  
953 several century-long increases in rainfall with complex responses of the environmental system – a  
954 result that favorably agrees with the climatic signal preserved by the speleothem record from  
955 Caverna Botuverá (Bernal et al., 2016b).

956 Future tasks to exploit this sediment record even further will link sedimentological and geochemical  
957 results with paleobiological data (Piraquive Bermúdez, 2020) to improve our understanding of  
958 interactions between regional vegetation and the geomorphological system in response to climate  
959 change. Remaining is the challenge of coring a longer sediment record from Lagoa Dourada with the  
960 ultimate goal to penetrate into the Pleistocene and to discover imprints of environmental changes  
961 linked to the Younger Dryas and the Antarctic Cold Reversal.

962

## 963 **Data Availability**

964 The multiproxy dataset of the lacustrine sediment record from Lagoa Dourada is accessible via the  
965 PANGAEA data archiving and publication system at  
966 <https://doi.pangaea.de/10.1594/PANGAEA.xxxxxx>. [The correct link will be provided during  
967 revisions.]

968

## 969 **Supplemental Material**

970 Supplementary figures and tables to this article are available online.

971

## 972 **Acknowledgements**

973 We are grateful to Vivian Luciana Jeske-Pieruschka (Universidade Federal do Ceará, Fortaleza, Brazil)  
974 for assistance in the field and organizing permits for the Vila Velha State Park. Support for sample  
975 preparation and analyses in the GEOPOLAR lab (University of Bremen) was provided by Carsten  
976 Smidt, Sabine Stahl and Rafael Stiens. Thanks also go to Hermann Behling (University of Göttingen)  
977 for support with field work and for critical comments on the draft as well as to Lujan Garcia  
978 (University of Bremen) for improving an earlier version of the manuscript. Finally, we acknowledge  
979 the constructive comments contributed by two anonymous reviewers. This research was funded by  
980 the Deutsche Forschungsgemeinschaft (DFG, German Research Foundation) as project GI 732/8-1.

981

## 982 **References**

- 983 Abdi, H., Williams, L.J., 2010. Principal Component Analysis. John Wiley & Sons, Ltd. .  
984 <http://dx.doi.org/https://doi.org/10.1002/wics.101>  
985 Aitchison, J., 1982. The statistical analysis of compositional data. Journal of the Royal Statistical  
986 Society. Series B: Statistical Methodology 44, 139–177.

987 Ayling, R.D., Martins, P.J., 1981. The growing of eucalypts on short rotation in Brazil. *The Forestry*  
988 *Chronicle* February 1981, 9-16.

989 Baker, P.A., Fritz, S.C., 2015. Nature and causes of Quaternary climate variation of tropical South  
990 America. *Quaternary Sci Rev* 124, 31-47. <http://dx.doi.org/10.1016/j.quascirev.2015.06.011>

991 Behling, H., 1995. A high resolution Holocene pollen record from Lago do Pires, SE Brazil: vegetation,  
992 climate and fire history. *Journal of Paleolimnology* 14, 253-268.

993 Behling, H., 2002. South and southeast Brazilian grasslands during Late Quaternary times: a synthesis.  
994 *Palaeogeogr Palaeocl* 177, 19-27. [http://dx.doi.org/Doi 10.1016/S0031-0182\(01\)00349-2](http://dx.doi.org/Doi 10.1016/S0031-0182(01)00349-2)

995 Behling, H., 2003. Late glacial and Holocene vegetation, climate and fire history inferred from Lagoa  
996 Nova in the southeastern Brazilian lowland. *Vegetation History and Archaeobotany* 12, 263-270.  
997 <http://dx.doi.org/10.1007/s00334-003-0020-9>

998 Behling, H., Oliveira, M.A.T.d., 2017. Evidence of a late glacial warming event and early Holocene  
999 cooling in the southern Brazilian coastal highlands. *Quaternary Research* 89, 90-102.  
1000 <http://dx.doi.org/10.1017/qua.2017.87>

1001 Behling, H., Pillar, V.D., Orlóci, L., Bauermann, S.G., 2004. Late Quaternary Araucaria forest, grassland  
1002 (Campos), fire and climate dynamics, studied by high-resolution pollen, charcoal and  
1003 multivariate analysis of the Cambará do Sul core in southern Brazil. *Palaeogeography,*  
1004 *Palaeoclimatology, Palaeoecology* 203, 277-297. [http://dx.doi.org/10.1016/s0031-](http://dx.doi.org/10.1016/s0031-0182(03)00687-4)  
1005 [0182\(03\)00687-4](http://dx.doi.org/10.1016/s0031-0182(03)00687-4)

1006 Behling, H., Safford, H.D., 2009. Late-glacial and Holocene vegetation, climate and fire dynamics in  
1007 the Serra dos Órgãos, Rio de Janeiro State, southeastern Brazil. *Global Change Biology* 16, 1661-  
1008 1671. <http://dx.doi.org/10.1111/j.1365-2486.2009.02029.x>

1009 Behling, H., Safford, H.D., 2010. Late-glacial and Holocene vegetation, climate and fire dynamics in  
1010 the Serra dos Órgãos, Rio de Janeiro State, southeastern Brazil. *Global Change Biology* 16, 1661-  
1011 1671. <http://dx.doi.org/10.1111/j.1365-2486.2009.02029.x>

1012 Bernal, J.P., Cruz, F.W., Strikis, N.M., Wang, X., Deininger, M., Catunda, M.C.A., Ortega-Obregón, C.,  
1013 Cheng, H., Edwards, R.L., Auler, A.S., 2016a. Botuverá Cave, Brazil - High-resolution Trace Metal  
1014 and Stable Isotope Speleothem Data covering the last 10,000 Years, 21.12.2016 ed.  
1015 <https://www.ncdc.noaa.gov/paleo/study/21060>

1016 Bernal, J.P., Cruz, F.W., Strikis, N.M., Wang, X., Deininger, M., Catunda, M.C.A., Ortega-Obregón, C.,  
1017 Cheng, H., Edwards, R.L., Auler, A.S., 2016b. High-resolution Holocene South American monsoon  
1018 history recorded by a speleothem from Botuverá Cave, Brazil. *Earth and Planetary Science*  
1019 *Letters* 450, 186-196. <http://dx.doi.org/10.1016/j.epsl.2016.06.008>

1020 Blaauw, M., Christen, J.A., Aquino Lopez, M.A., 2021. rbacon: Age-Depth Modelling using Bayesian  
1021 Statistics, R package version 2.5.1. ed.

1022 Blott, S.J., Pye, K., 2001. GRADISTAT: a grain size distribution and statistics package for the analysis of  
1023 unconsolidated sediments. *Earth Surface Processes and Landforms* 26, 1237-1248.  
1024 <http://dx.doi.org/10.1002/esp.261>

1025 Bradley, R.S., Bakke, J., 2019. Is there evidence for a 4.2 ka BP event in the northern North Atlantic  
1026 region? *Clim Past* 15, 1665-1676. <http://dx.doi.org/10.5194/cp-15-1665-2019>

1027 Bronk Ramsey, C., 2009. Bayesian analysis of radiocarbon dates. *Radiocarbon* 51, 337-360.

1028 Carnaval, A.C., Hickerson, M.J., Haddad, C.F.B., Rodrigues, M.T., Moritz, C., 2009. Stability Predicts  
1029 Genetic Diversity in the Brazilian Atlantic Forest Hotspot. *Science* 323, 785-789.  
1030 <http://dx.doi.org/10.1126/science.1166955>

1031 Croudace, I.W., Löwemark, L., Tjallingii, R., Zolitschka, B., 2019. Current perspectives on the  
1032 capabilities of high resolution XRF core scanners. *Quatern Int* 514, 5-15.  
1033 <http://dx.doi.org/10.1016/j.quaint.2019.04.002>

1034 Croudace, I.W., Rindby, A., Rothwell, R.G., 2006. ITRAX: description and evaluation of a new multi-  
1035 function X-ray core scanner, in: Rothwell, R.G. (Ed.), *New techniques in sediment core analysis.*  
1036 *The Geological Society of London Special Publications*, London, pp. 51-63.

1037 Croudace, I.W., Rothwell, R.G., 2015. Future Developments and Innovations in High-Resolution Core  
1038 Scanning. *Dev Paleoenviron Res* 17, 627-647. [http://dx.doi.org/10.1007/978-94-017-9849-5\\_27](http://dx.doi.org/10.1007/978-94-017-9849-5_27)

1039 Cruz, F.W., Burns, S.J., Jercinovic, M., Karmann, I., Sharp, W.D., Vuille, M., 2007. Evidence of rainfall  
1040 variations in Southern Brazil from trace element ratios (Mg/Ca and Sr/Ca) in a Late Pleistocene  
1041 stalagmite. *Geochimica et Cosmochimica Acta* 71, 2250-2263.  
1042 <http://dx.doi.org/10.1016/j.gca.2007.02.005>

1043 Cruz, F.W., Burns, S.J., Karmann, I., Sharp, W.D., Vuille, M., Cardoso, A.O., Ferrari, J.A., Silva Dias, P.L.,  
1044 Viana Jr, O., 2005. Insolation-driven changes in atmospheric circulation over the past 116,000  
1045 years in subtropical Brazil. *Nature* 434, 63-66. <http://dx.doi.org/10.1029/>  
1046 Cruz, F.W., et al., 2005. Botuverá Cave, Brazil Stalagmite Stable Isotope Data, 03/2005 ed. IGBP  
1047 PAGES/World Data Center for Paleoclimatology, Data Contribution Series # 2005-027,  
1048 NOAA/NCDC Paleoclimatology Program, Boulder CO, USA.

1049 Cruz, F.W., Vuille, M., Burns, S.J., Wang, X., Cheng, H., Werner, M., Lawrence Edwards, R., Karmann,  
1050 I., Auler, A.S., Nguyen, H., 2009. Orbitally driven east–west antiphasing of South American  
1051 precipitation. *Nat Geosci* 2, 210-214. <http://dx.doi.org/10.1038/ngeo444>

1052 Dean, W.E., 1974. Determination of Carbonate and Organic-Matter in Calcareous Sediments and  
1053 Sedimentary-Rocks by Loss on Ignition - Comparison with Other Methods. *Journal of*  
1054 *Sedimentary Petrology* 44, 242-248.

1055 Dearing, J., 1994. Environmental magnetic susceptibility: using the Bartington MS2 system. Chi  
1056 Publishing, Kenilworth.

1057 Deininger, M., McDermott, F., Cruz, F.W., Bernal, J.P., Mudelsee, M., Vonhof, H., Millo, C., Spotl, C.,  
1058 Treble, P.C., Pickering, R., Scholz, D., 2020. Inter-hemispheric synchronicity of Holocene  
1059 precipitation anomalies controlled by Earth's latitudinal insolation gradients. *Nat Commun* 11,  
1060 5447. <http://dx.doi.org/10.1038/s41467-020-19021-3>

1061 Deininger, M., Ward, B.M., Novello, V.F., Cruz, F.W., 2019. Late Quaternary Variations in the South  
1062 American Monsoon System as Inferred by Speleothems—New Perspectives using the SISAL  
1063 Database. *Quaternary* 2. <http://dx.doi.org/10.3390/quat2010006>

1064 Enters, D., Behling, H., Mayr, C., Dupont, L., Zolitschka, B., 2010. Holocene environmental dynamics  
1065 of south-eastern Brazil recorded in laminated sediments of Lago Aleixo. *Journal of*  
1066 *Paleolimnology* 44, 265-277. <http://dx.doi.org/10.1007/s10933-009-9402-z>

1067 Folk, R.L., Ward, W.C., 1957. Brazos river bar: a study in the significance of grain size parameters.  
1068 *Journal of Sedimentary Petrology* 27, 3-26.

1069 Freitas, F., 2011. Land Use and Deforestation in Southeastern Brazil — 1753-1840, pp.  
1070 [https://fredericofreitas.org/2011/2011/2018/land-use-and-deforestation-in-southeastern-brazil-](https://fredericofreitas.org/2011/2011/2018/land-use-and-deforestation-in-southeastern-brazil-1753-1840/#f2011)  
1071 [1753-1840/#f2011](https://fredericofreitas.org/2011/2011/2018/land-use-and-deforestation-in-southeastern-brazil-1753-1840/#f2011).

1072 Giesche, A., Staubwasser, M., Petrie, C.A., Hodell, D.A., 2019. Indian winter and summer monsoon  
1073 strength over the 4.2 ka BP event in foraminifer isotope records from the Indus River delta in the  
1074 Arabian Sea. *Clim Past* 15, 73-90. <http://dx.doi.org/10.5194/cp-15-73-2019>

1075 Governo do Estado de Paraná, 2004. Plano de Manejo Parque Estadual de Vila Velha.

1076 Goldberg, A., Mychajliw, A.M., Hadly, E.A., 2016. Post-invasion demography of prehistoric humans in  
1077 South America. *Nature* 532, 232-235. <http://dx.doi.org/10.1038/nature17176>

1078 Harris, C.R., Millman, K.J., van der Walt, S.J., Gommers, R., Virtanen, P., Cournapeau, D., Wieser, E.,  
1079 Taylor, J., Berg, S., Smith, N.J., Kern, R., Picus, M., Hoyer, S., van Kerkwijk, M.H., Brett, M.,  
1080 Haldane, A., del Río, J.F., Wiebe, M., Peterson, P., Gérard-Marchant, P., Sheppard, K., Reddy, T.,  
1081 Weckesser, W., Abbasi, H., Gohlke, C., Oliphant, T.E., 2020. Array programming with NumPy.  
1082 *Nature* 585, 357-362. <http://dx.doi.org/10.1038/s41586-020-2649-2>

1083 Hogg, A., Heaton, T., Hua, Q., Palmer, J., Turney, C., Southon, J., Bayliss, A., Blackwe Boswijk, G.,  
1084 Bronk Ramsey, C., Pearson, C., Petchey, F., Reimer, P., Reimer, R., Wacker, L., 2020. SHCal20  
1085 Southern Hemisphere calibration, 0-55,000 years cal BP. *Radiocarbon* 62. [http://dx.doi.org/doi:](http://dx.doi.org/doi:10.1017/RDC.2020.59)  
1086 [10.1017/RDC.2020.59](http://dx.doi.org/doi:10.1017/RDC.2020.59)

1087 Huguén, K.A., Overpeck, J.T., Peterson, L.C., Trumbore, S., 1996. Rapid climate changes in the tropical  
1088 Atlantic region during the last deglaciation. *Nature* 380, 51-54.  
1089 <http://dx.doi.org/10.1038/380051a0>



1090 Hunter, J.D., 2007. Matplotlib: A 2D Graphics Environment. *Computing in Science and Engineering* 9,  
1091 99–104.

1092 Jaqueto, P., Trindade, R.I.F., Hartmann, G.A., Novello, V.F., Cruz, F.W., Karmann, I., Strauss, B.E.,  
1093 Feinberg, J.M., 2016. Linking speleothem and soil magnetism in the Pau d’Alho cave (central  
1094 South America). *Journal of Geophysical Research: Solid Earth* 121.  
1095 <http://dx.doi.org/doi:10.1002/2016JB013541>

1096 Jeske-Pieruschka, V., Pillar, V.D., De Oliveira, M.A.T., Behling, H., 2013. New insights into vegetation,  
1097 climate and fire history of southern Brazil revealed by a 40,000 year environmental record from  
1098 the State Park Serra do Tabuleiro. *Vegetation History and Archaeobotany* 22, 299-314.  
1099 <http://dx.doi.org/10.1007/s00334-012-0382-y>

1100 Kathayat, G., Cheng, H., Sinha, A., Berkelhammer, M., Zhang, H., Duan, P., Li, H., Li, X., Ning, Y.,  
1101 Edwards, R.L., 2018. Evaluating the timing and structure of the 4.2 ka event in the Indian  
1102 summer monsoon domain from an annually resolved speleothem record from Northeast India.  
1103 *Clim Past* 14, 1869-1879. <http://dx.doi.org/10.5194/cp-14-1869-2018>

1104 Ledru, M.-P., Mourguiart, P., Riccomini, C., 2009. Related changes in biodiversity, insolation and  
1105 climate in the Atlantic rainforest since the last interglacial. *Palaeogeography, Palaeoclimatology,*  
1106 *Palaeoecology* 271, 140-152. <http://dx.doi.org/10.1016/j.palaeo.2008.10.008>

1107 Ledru, M.-P., Salgado-Labouriau, M.L., Lorscheitter, M.L., 1998. Vegetation dynamics in southern and  
1108 central Brazil during the last 10,000 yr B.P. *Review of Palaeobotany and Palynology* 99, 131-142.

1109 Liu, X., Colman, S.M., Brown, E.T., Minor, E.C., Li, H., 2013. Estimation of carbonate, total organic  
1110 carbon, and biogenic silica content by FTIR and XRF techniques in lacustrine sediments. *Journal*  
1111 *of Paleolimnology* 50, 387-398. <http://dx.doi.org/10.1007/s10933-013-9733-7>

1112 Lorscheitter, M.L., Takeda, I.J.M., 1995. Reconstituição paleoambiental da região dos Campos Gerais,  
1113 Paraná, através da palinologia de sedimentos da Lagoa Dourada, V Congresso da Associação  
1114 Brasileira de Estudos do Quaternário, XI Simpósio de Sedimentologia Costeira, . Anais. Niterói,  
1115 ABEQUA, 18-21, Niterói, RJ, pp. 18-21.

1116 Löwemark, L., Bloemsma, M., Croudace, I., Daly, J.S., Edwards, R.J., Francus, P., Galloway, J.M.,  
1117 Gregory, B.R.B., Steven Huang, J.-J., Jones, A.F., Kylander, M., Löwemark, L., Luo, Y., Maclachlan,  
1118 S., Ohlendorf, C., Patterson, R.T., Pearce, C., Profe, J., Reinhardt, E.G., Stranne, C., Tjallingii, R.,  
1119 Turner, J.N., 2019. Practical guidelines and recent advances in the Itrax XRF core-scanning  
1120 procedure. *Quatern Int* 514, 16-29. <http://dx.doi.org/10.1016/j.quaint.2018.10.044>

1121 Martin-Puertas, C., Tjallingii, R., Bloemsma, M., Brauer, A., 2017. Varved sediment responses to early  
1122 Holocene climate and environmental changes in Lake Meerfelder Maar (Germany) obtained  
1123 from multivariate analyses of micro X-ray fluorescence core scanning data. *Journal of Quaternary*  
1124 *Science* 32, 427-436. <http://dx.doi.org/10.1002/jqs.2935>

1125 McInnes, L., Healy, J., Astels, S., 2017. Hdbscan: Hierarchical Density Based Clustering. *The Journal of*  
1126 *Open Source Software* 2, 205.  
1127 <http://dx.doi.org/http://joss.theoj.org/papers/10.21105/joss.00205>

1128 Melo, M.S., Giannini, P.C.F., Pessenda, L.C.R., Neto Brandt, M., 2003. Holocene paleoclimatic  
1129 reconstruction based on the Lagoa Dourada deposits, southern Brazil. *Geologica Acta: an*  
1130 *international Earth science journal* 1, 289-302.

1131 Melo, M.S.d., Coimbra, A.M., 1996. Ruiniform relief in sandstones: the example of Vila Velha,  
1132 Carboniferous of the Parana Basin, Southern Brazil. *Acta Geologica Hispanica* 31, 25-40.

1133 Melo, M.S.d., Giannini, P.C.F., 2007. Sandstone dissolution landforms in the Furnas Formation,  
1134 southern Brazil. *Earth Surface Processes and Landforms* 32, 2149-2164.  
1135 <http://dx.doi.org/10.1002/esp.1520>

1136 Merkel, A., 2020. Climate data of Ponta Grossa, Brasil [www.climate-](http://www.climate-data.org/suedamerika/brasilien/parana/ponta-grossa-4493/)  
1137 [data.org/suedamerika/brasilien/parana/ponta-grossa-4493/](http://www.climate-data.org/suedamerika/brasilien/parana/ponta-grossa-4493/).

1138 Meyers, P.A., Teranes, J.L., 2001. Sediment Organic Matter, in: Last, W.M., Smol, J.P. (Eds.), *Tracking*  
1139 *Environmental Change Using Lake Sediments. Volume 2: Physical and Geochemical Methods.*  
1140 Kluwer Academic Publishers, Dordrecht, pp. 239-269.

- 1141 Moro, R.S., de Mattos Bicudo, C.E., de Melo, M.S., Schmitt, J., 2004. Paleoclimate of the late  
 1142 Pleistocene and Holocene at Lagoa Dourada, Paraná State, southern Brazil. *Quatern Int* 114, 87-  
 1143 99. [http://dx.doi.org/10.1016/s1040-6182\(03\)00044-2](http://dx.doi.org/10.1016/s1040-6182(03)00044-2)
- 1144 Moro, R.S., Fürstenberger, C.B., 1998. Inferring lakewater characteristics in Lagoa Dourada, PR, Brazil,  
 1145 from surface sediment diatom assemblage data. *Internationale Vereinigung für theoretische und*  
 1146 *angewandte Limnologie: Verhandlungen* 26, 1755-1757.  
 1147 <http://dx.doi.org/10.1080/03680770.1995.11901037>
- 1148 Morrill, C., LeGrande, A.N., Renssen, H., Bakker, P., Otto-Bliesner, B.L., 2013. Model sensitivity to  
 1149 North Atlantic freshwater forcing at 8.2 ka. *Clim Past* 9, 955–968.
- 1150 Müller, P.J., Schneider, R., 1993. An automated leaching method for the determination of opal in  
 1151 sediments and particulate matter. *Deep Sea Research Part I: Oceanographic Research Papers* 40,  
 1152 425-444.
- 1153 Myers, N., Mittermeier, R.A., Mittermeier, C.G., Fonseca, G.A.B.d., Kent, J., 2000. Biodiversity  
 1154 hotspots for conservation priorities. *Nature* 403, 853–858.
- 1155 Nesje, A., Søgne, K., Elgersma, A., Dahl, S.O., 1987. A Piston Corer for Lake Sediments. *Norsk*  
 1156 *Geografisk Tidsskrift - Norwegian Journal of Geography* 41, 123-125.  
 1157 <http://dx.doi.org/https://doi.org/10.1080/00291958708621986>
- 1158 Novello, V.F., Cruz, F.W., Vuille, M., Strikis, N.M., Edwards, R.L., Cheng, H., Emerick, S., de Paula, M.S.,  
 1159 Li, X., Barreto, E.S., Karmann, I., Santos, R.V., 2017. A high-resolution history of the South  
 1160 American Monsoon from Last Glacial Maximum to the Holocene. *Sci Rep* 7, 44267.  
 1161 <http://dx.doi.org/10.1038/srep44267>
- 1162 Novello, V.F., William da Cruz, F., Vuille, M., Pereira Silveira Campos, J.L., Strikis, N.M., Apaéstegui, J.,  
 1163 Moquet, J.S., Azevedo, V., Ampuero, A., Utida, G., Wang, X., Paula-Santos, G.M., Jaqueto, P., Ruiz  
 1164 Pessenda, L.C., Breecker, D.O., Karmann, I., 2021. Investigating  $\delta^{13}C$  values in stalagmites from  
 1165 tropical South America for the last two millennia. *Quaternary Sci Rev* 255.  
 1166 <http://dx.doi.org/10.1016/j.quascirev.2021.106822>
- 1167 Nowaczyk, N.R., 2001. Logging of magnetic susceptibility, in: Last, W.M., Smol, J.P. (Eds.), *Tracking*  
 1168 *environmental changes using lake sediments. Volume 1: Basin analysis, coring, and chronological*  
 1169 *techniques. Kluwer Academic Publishers, Dordrecht, The Netherlands, pp. 155-170.*
- 1170 Pedregosa, F., Varoquaux, G., Gramfort, A., Michel, V., Thirion, B., Grisel, O., Blondel, M., 2011. Scikit-  
 1171 Learn: Machine Learning in Python. *Journal of Machine Learning Research* 12, 2825–2830.
- 1172 Piraquive Bermúdez, D., 2020. Vegetation and fire history in Araucaria forest and grasslands,  
 1173 southern Brazil, Doctoral Thesis, University of Göttingen,144.
- 1174 Piraquive Bermúdez, D., Theuerkauf, M., Giesecke, T., 2021. Towards quantifying changes in forest  
 1175 cover in the Araucaria forest-grassland mosaic in southern Brazil. *Vegetation History and*  
 1176 *Archaeobotany*. <http://dx.doi.org/https://doi.org/10.1007/s00334-021-00841-2>
- 1177 Pires, L.F., Melo, M.S.d., Borges, J.A.R., Heck, R.J., Facin, P.C., 2019. X-ray Microtomography to  
 1178 Quantify Morphological Sandstones Properties. *Brazilian Archives of Biology and Technology* 62,  
 1179 e19180125. <http://dx.doi.org/10.1590/1678-4324-2019180125>
- 1180 Pontes, H., Fernandes, L., de Melo, M., Guimarães, G., Massuqueto, L., 2020. Speleothems in quartz-  
 1181 sandstone caves of Ponta Grossa municipality, Campos Gerais region, Paraná state, southern  
 1182 Brazil. *International Journal of Speleology* 49, 119-136. <http://dx.doi.org/10.5038/1827-806x.49.2.2313>
- 1183
- 1184 Portes, M.C.G.d.O., Safford, H., Behling, H., 2018. Humans and climate as designers of the landscape  
 1185 in Serra da Bocaina National Park, southeastern Brazil, over the last seven centuries.  
 1186 *Anthropocene* 24, 61-71. <http://dx.doi.org/10.1016/j.ancene.2018.11.004>
- 1187 Riris, P., Arroyo-Kalin, M., 2019. Widespread population decline in South America correlates with  
 1188 mid-Holocene climate change. *Sci Rep* 9, 6850. <http://dx.doi.org/10.1038/s41598-019-43086-w>
- 1189 Rodrigues-Filho, S., Behling, H., Irion, G., Müller, G., 2002. Evidence for Lake Formation as a Response  
 1190 to an Inferred Holocene Climatic Transition in Brazil. *Quaternary Research* 57, 131-137.  
 1191 <http://dx.doi.org/10.1006/qres.2001.2281>

1192 Rodrigues, J.M., Behling, H., Giesecke, T., 2016. Holocene dynamics of vegetation change in southern  
1193 and southeastern Brazil is consistent with climate forcing. *Quaternary Sci Rev* 146, 54-65.  
1194 <http://dx.doi.org/10.1016/j.quascirev.2016.06.011>

1195 Rothwell, R.G., 1989. *The Smear Slide Method - An Optical Identification Guide*. Springer, Dordrecht.  
1196 [http://dx.doi.org/https://doi.org/10.1007/978-94-009-1133-8\\_2](http://dx.doi.org/https://doi.org/10.1007/978-94-009-1133-8_2)

1197 Scuderi, L.A., Yang, X., Ascoli, S.E., Li, H., 2019. The 4.2 ka BP Event in northeastern China: a  
1198 geospatial perspective. *Clim Past* 15, 367-375. <http://dx.doi.org/10.5194/cp-15-367-2019>

1199 Soares Cruz, A.P., Fernandes Barbosa, C., Blanco, A.M., de Oliveira, C.A., Guizan Silva, C., Sícoli  
1200 Seoane, J.C., 2019. Mid-late Holocene event registered in organo-siliciclastic sediments of Lagoa  
1201 Salgada carbonate system, southeast Brazil. *Clim Past* 15, 1363-1373.  
1202 <http://dx.doi.org/10.5194/cp-15-1363-2019>

1203 Suguio, K., Turcq, B., Servant, M., Soubiös, F., Fournier, M., 1989. Holocene fluvial deposits in  
1204 southeast Brazil: chronology and palaeohydrological implications, *International Symposium*  
1205 *on Global Changes in South America During the Quaternary*, 7G-73, São Paulo (Brazil), pp. 70-74.

1206 Thomaz, G.M., 2010. Vila Velha State Park, Brazil: Curious and Very Interesting Sandstone  
1207 Formations, pp. <https://traveltoparana.wordpress.com/2010/2005/2006/parque-estadual-de->  
1208 [vila-velha-state-park-parana-brazil/](https://traveltoparana.wordpress.com/2010/2005/2006/parque-estadual-de-).

1209 Tjallingii, R., Röhl, U., Kölling, M., Bickert, T., 2007. Influence of the water content on X-ray  
1210 fluorescence core-scanning measurements in soft marine sediments. *Geochemistry, Geophysics,*  
1211 *Geosystems* 8, 1-12. <http://dx.doi.org/doi:10.1029/2006GC001393>

1212 Utida, G., Cruz, F.W., Santos, R.V., Sawakuchi, A.O., Wang, H., Pessenda, L.C.R., Novello, V.F., Vuille,  
1213 M., Strauss, A.M., Borella, A.C., Stríkis, N.M., Guedes, C.C.F., Dias De Andrade, F.R., Zhang, H.,  
1214 Cheng, H., Edwards, R.L., 2020. Climate changes in Northeastern Brazil from deglacial to  
1215 Meghalayan periods and related environmental impacts. *Quaternary Sci Rev* 250, 106655.  
1216 <http://dx.doi.org/10.1016/j.quascirev.2020.106655>

1217 van der Walt, S., Schönberger, J., Nunez-Iglesias, J., Boulogne, F., Warner, J., Yager, N., Gouillart, E.,  
1218 Yu, T., the scikit-image contributors, 2014. scikit-image: image processing in Python. *PeerJ* 2,  
1219 e453. <http://dx.doi.org/https://doi.org/10.7717/peerj.453>

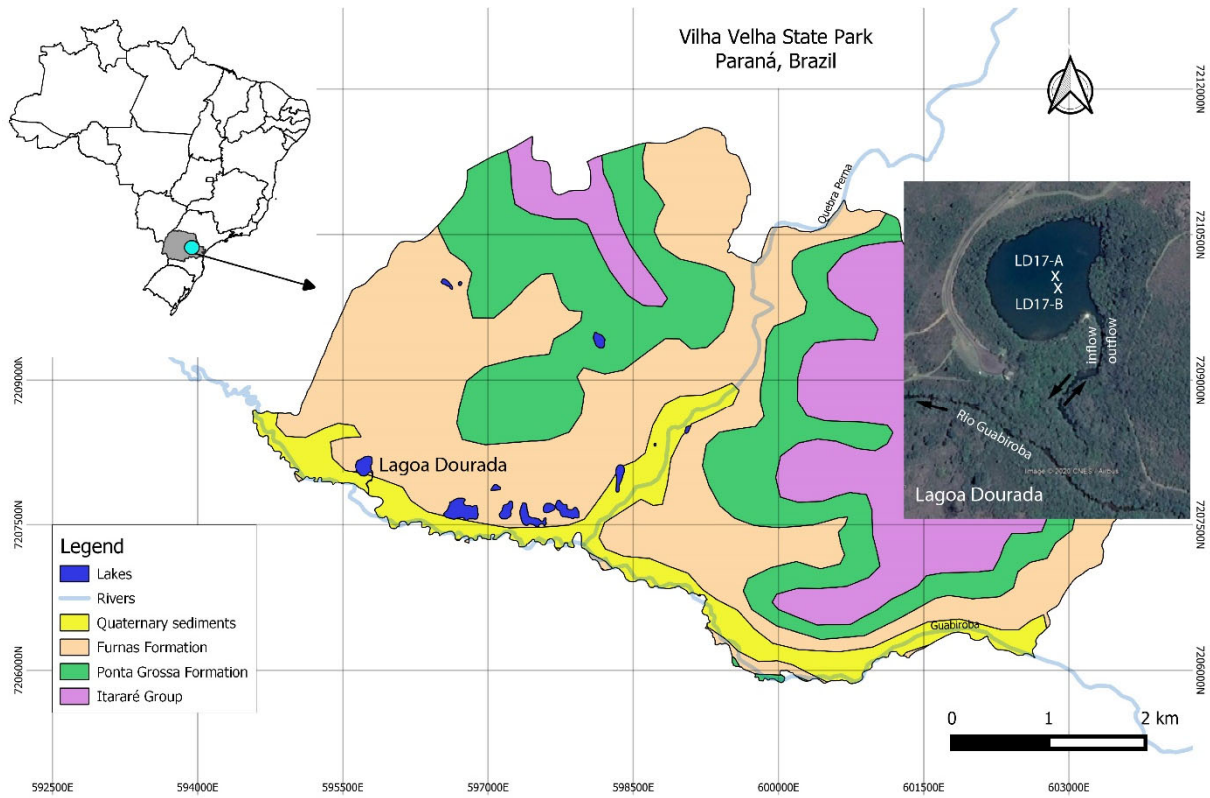
1220 Virtanen, P., Gommers, R., Oliphant, T.E., Haberland, M., Reddy, T., Cournapeau, D., Burovski, E.,  
1221 Peterson, P., Weckesser, W., Bright, J., van der Walt, S.J., Brett, M., Wilson, J., Millman, K.J.,  
1222 Mayorov, N., Nelson, A.R.J., Jones, E., Kern, R., Larson, E., Carey, C.J., Polat, İ., Feng, Y., Moore,  
1223 E.W., VanderPlas, J., Laxalde, D., Perktold, J., Cimrman, R., Henriksen, I., Quintero, E.A., Harris,  
1224 C.R., Archibald, A.M., Ribeiro, A.H., Pedregosa, F., van Mulbregt, P., Vijaykumar, A., Bardelli, A.P.,  
1225 Rothberg, A., Hilboll, A., Kloeckner, A., Scopatz, A., Lee, A., Rokem, A., Woods, C.N., Fulton, C.,  
1226 Masson, C., Häggström, C., Fitzgerald, C., Nicholson, D.A., Hagen, D.R., Pasechnik, D.V., Olivetti,  
1227 E., Martin, E., Wieser, E., Silva, F., Lenders, F., Wilhelm, F., Young, G., Price, G.A., Ingold, G.-L.,  
1228 Allen, G.E., Lee, G.R., Audren, H., Probst, I., Dietrich, J.P., Silterra, J., Webber, J.T., Slavič, J.,  
1229 Nothman, J., Buchner, J., Kulick, J., Schönberger, J.L., de Miranda Cardoso, J.V., Reimer, J.,  
1230 Harrington, J., Rodríguez, J.L.C., Nunez-Iglesias, J., Kuczynski, J., Tritz, K., Thoma, M., Newville,  
1231 M., Kümmerer, M., Bolingbroke, M., Tartre, M., Pak, M., Smith, N.J., Nowaczyk, N., Shebanov, N.,  
1232 Pavlyk, O., Brodtkorb, P.A., Lee, P., McGibbon, R.T., Feldbauer, R., Lewis, S., Tygier, S., Sievert, S.,  
1233 Vigna, S., Peterson, S., More, S., Pudlik, T., Oshima, T., Pingel, T.J., Robitaille, T.P., Spura, T.,  
1234 Jones, T.R., Cera, T., Leslie, T., Zito, T., Krauss, T., Upadhyay, U., Halchenko, Y.O., Vázquez-Baeza,  
1235 Y., SciPy, C., 2020. SciPy 1.0: fundamental algorithms for scientific computing in Python. *Nature*  
1236 *Methods* 17, 261-272. <http://dx.doi.org/10.1038/s41592-019-0686-2>

1237 Wang, X., Auler, A.S., Edwards, R.L., Cheng, H., Ito, E., Wang, Y., Kong, X., Solheid, M., 2007.  
1238 Millennial-scale precipitation changes in southern Brazil over the past 90,000 years. *Geophys Res*  
1239 *Lett* 34, n/a-n/a. <http://dx.doi.org/10.1029/2007gl031149>

1240 Weltje, G., Bloemsma, M., Tjallingii, R., Heslop, D., Röhl, U., Croudace, I., 2015. Prediction of  
1241 Geochemical Composition from XRF Core Scanner Data: A New Multivariate Approach Including  
1242 Automatic Selection of Calibration Samples and Quantification of Uncertainties, in: Croudace, I.,

- 1243 Rothwell, R. (Eds.), *Micro-XRF Studies of Sediment Cores*. Springer, Dordrecht, pp. 507-534.  
1244 [http://dx.doi.org/https://doi.org/10.1007/978-94-017-9849-5\\_21](http://dx.doi.org/https://doi.org/10.1007/978-94-017-9849-5_21)
- 1245 Weltje, G.J., Tjallingii, R., 2008. Calibration of XRF core scanners for quantitative geochemical logging  
1246 of sediment cores: Theory and application. *Earth and Planetary Science Letters* 274, 423-438.  
1247 <http://dx.doi.org/10.1016/j.epsl.2008.07.054>
- 1248 Woodward, C.A., Gadd, P.S., 2019. The potential power and pitfalls of using the X-ray fluorescence  
1249 molybdenum incoherent: Coherent scattering ratio as a proxy for sediment organic content.  
1250 *Quatern Int* 514, 30-43. <http://dx.doi.org/10.1016/j.quaint.2018.11.031>
- 1251 Wray, R.A.L., 2013. Solutional weathering and karstic landscapes on quartz sandstones and quartzite,  
1252 in: Frumkin, A. (Ed.), *Treatise on Geomorphology*. Academic Press, San Diego, pp. 463-483.
- 1253 Wright, H.E., 1967. A square-rod piston sampler for lake sediments. *Journal of Sedimentary Research*  
1254 37, 975-976. [http://dx.doi.org/https://doi.org/10.1306/74D71807-2B21-11D7-  
1255 8648000102C1865D](http://dx.doi.org/https://doi.org/10.1306/74D71807-2B21-11D7-8648000102C1865D)
- 1256 Zhou, J., Lau, K.-M., 1998. Does a Monsoon Climate Exist over South America? *J Climate* 11, 1020-  
1257 1040.
- 1258 Zolitschka, B., 1998. A 14,000 year sediment yield record from Western Germany based on annually  
1259 laminated sediments. *Geomorphology* 22, 1-17.
- 1260 Zolitschka, B., Fey, M., Janssen, S., Maidana, N.I., Mayr, C., Wulf, S., Haberzettl, T., Corbella, H., Lücke,  
1261 A., Ohlendorf, C., Schäbitz, F., 2019. Southern Hemispheric Westerlies control sedimentary  
1262 processes of Laguna Azul (south-eastern Patagonia, Argentina). *The Holocene* 29, 403-420.  
1263 <http://dx.doi.org/10.1177/0959683618816446>
- 1264  
1265

1266



1267

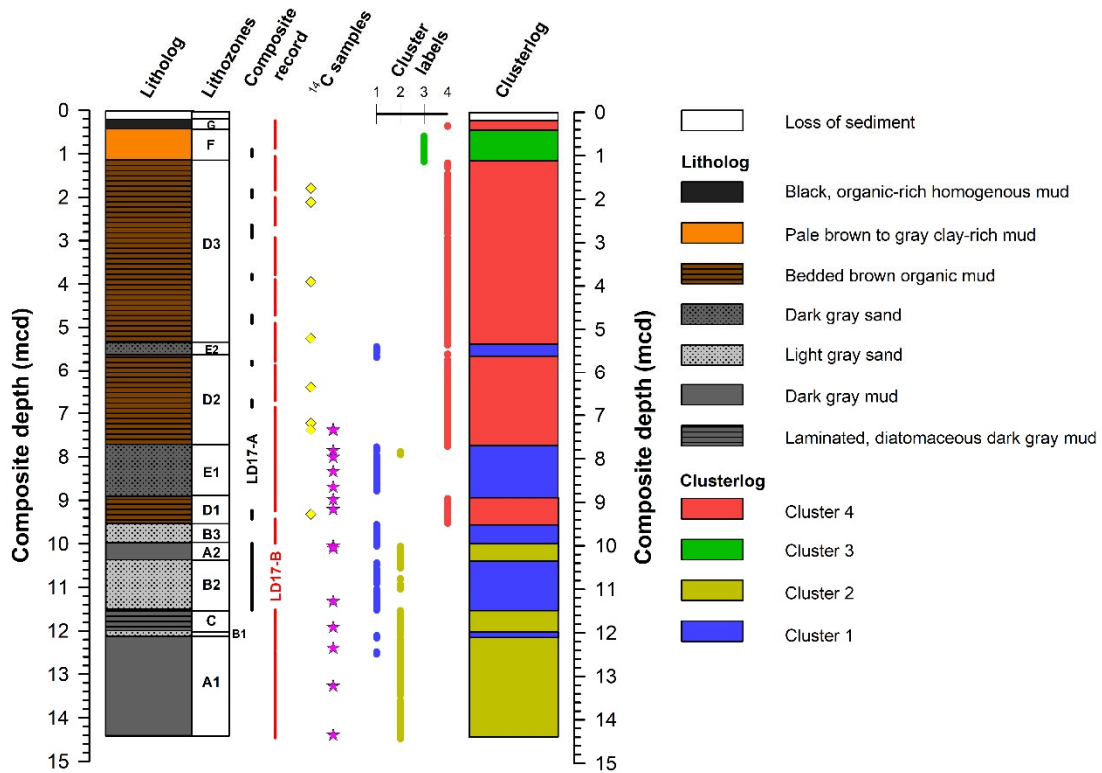
1268 Fig. 1: Location of Lagoa Dourada in Paraná (South Brazil) with a geological map of the Vilha Velha  
1269 State Park based on information from “Plano de Manejo Vegetação Parque Estadual Vila Velha”  
1270 (Governo do Estado de Paraná, 2004) and an aerial photography of the lake with Rio Guabirola from  
1271 Google Earth. Coring locations LD17-A and LD17-B are marked (X) in the aerial photography.

1272

1273

1274

1275



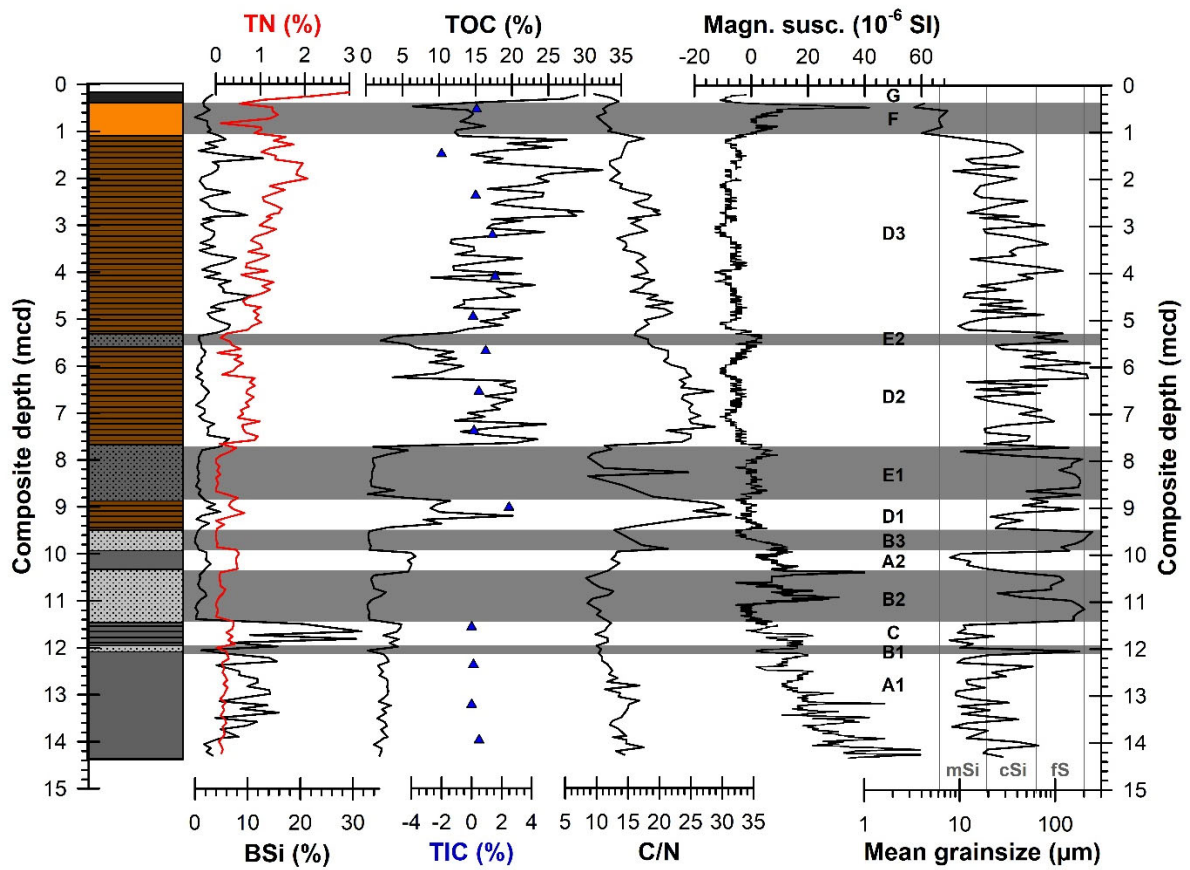
1276

1277 Fig. 2: Litholog (left) of the composite record based on macroscopic and microscopic observations  
 1278 with lithozones A1 through G, core sections used for the construction of the composite record as well  
 1279 as positions of samples for radiocarbon (<sup>14</sup>C) dating. Radiocarbon ages of terrestrial macrofossils are  
 1280 shown as yellow diamonds and those on bulk organic matter as pink stars. All data related to <sup>14</sup>C  
 1281 dating are provided with Tab. 1. Clusterlog (right) is based on cluster analysis for comparison.

1282

1283

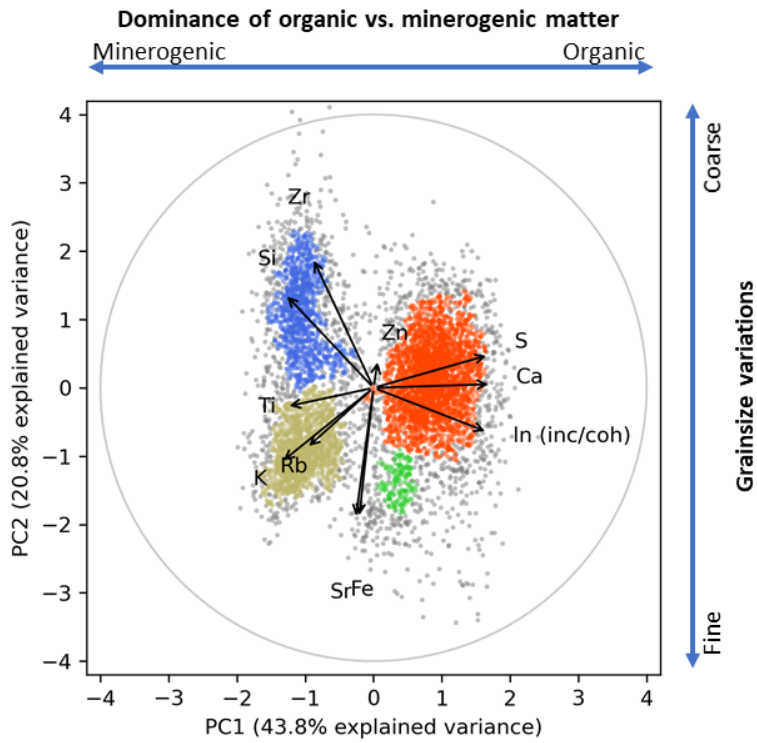
1284



1285

1286 Fig. 3: Litholog with lithozones A1 through G (for legend: cf., Fig. 2) with bulk geochemistry, including  
 1287 total nitrogen (TN), total organic carbon (TOC), total inorganic carbon (TIC), magnetic susceptibility  
 1288 (Magn. susc.), biogenic silica (BSi), carbon-to-nitrogen ratio (C/N) and mean grainsize. Sand horizons  
 1289 (LZs B and E) and lithozone F are shaded in gray.

1290

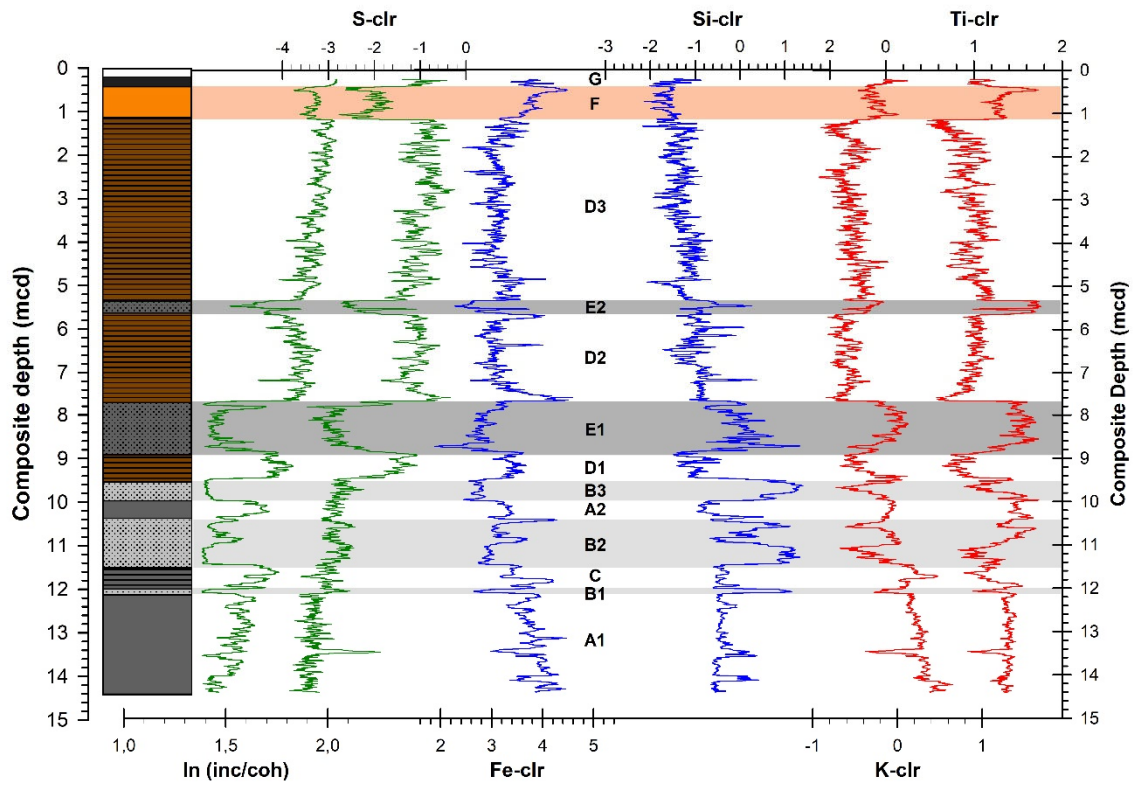


1291

1292 Fig. 4: PCA loadings from homogenized (clr-transformed) elemental intensities obtained by XRF core  
 1293 scanning. The first two principal components preserve 64.6 % of the total variance. The four  
 1294 determined clusters (Cluster 1-4) are color-coded (for legend: cf., Fig. 2) and data points related to  
 1295 noise are plotted in gray. The circle indicates a value of 1 for the loadings. Interpretations in terms of  
 1296 grainsize variations and dominance of organic vs. minerogenic matter are indicated by blue arrows.

1297



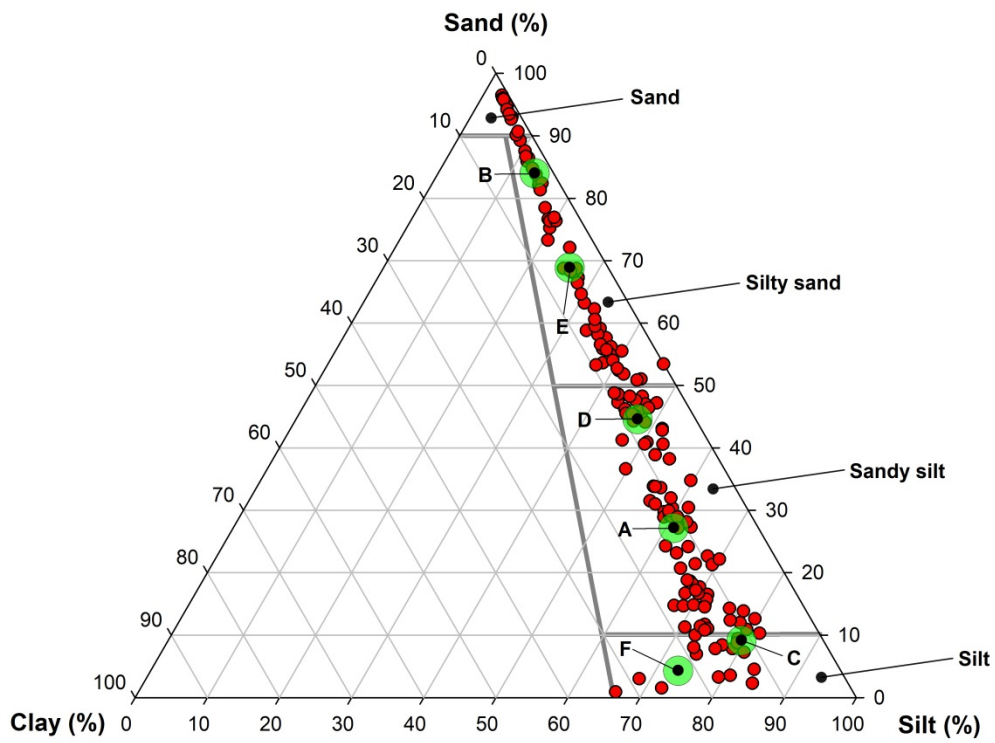


1298

1299 Fig. 5: Litholog with lithozones A1 through G (for legend: cf., Fig. 2) and selected clr-transformed  
 1300 elemental data obtained by XRF core scanning. Shown are the elements sulphur (S), silica (Si),  
 1301 titanium (Ti), iron (Fe), potassium (K) and the incoherent/coherent ratio (inc/coh). Sand horizons (LZs  
 1302 B and E) and lithozone F are shaded in gray.

1303

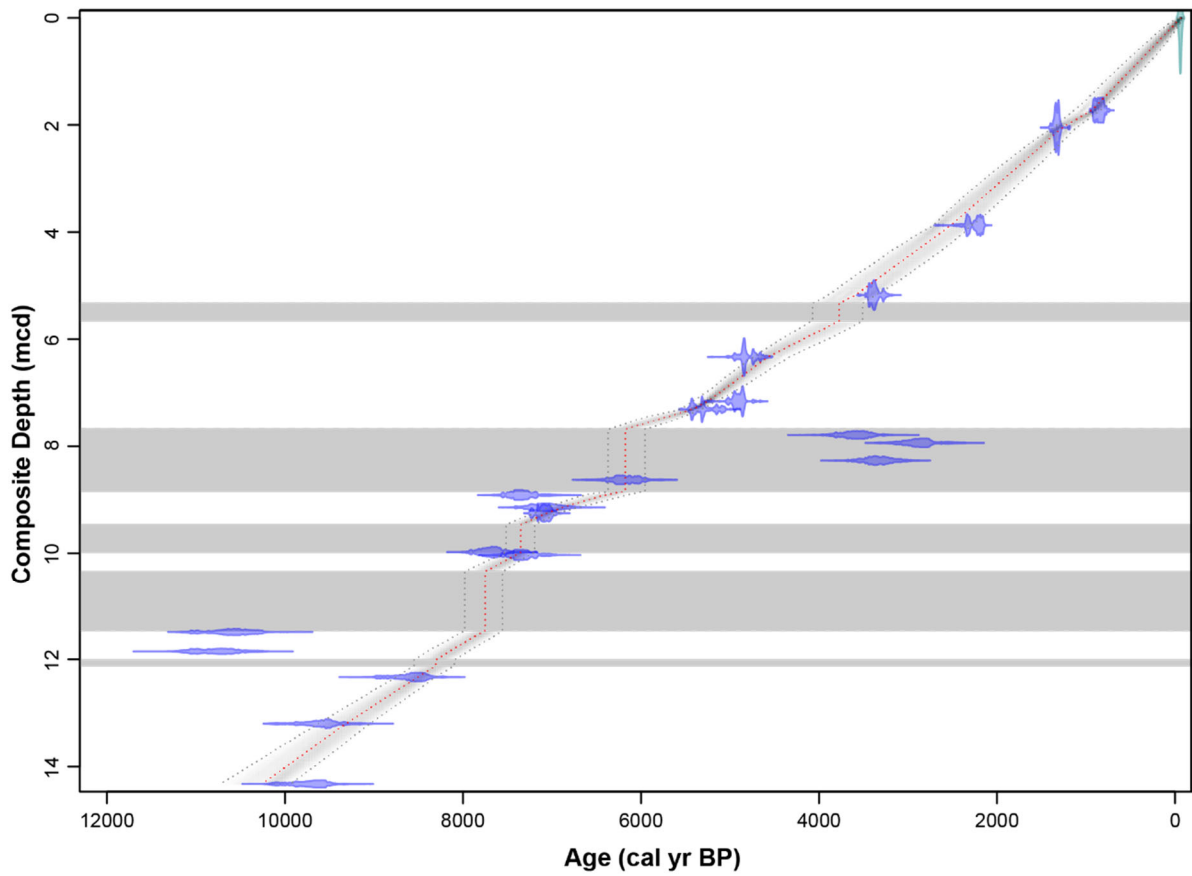
1304



1305

1306 Fig. 6: Ternary grainsize diagram (red dots mark individual samples) with mean grainsize values for  
 1307 lithozones A-F (labeled with the corresponding letter and encircled in green color).

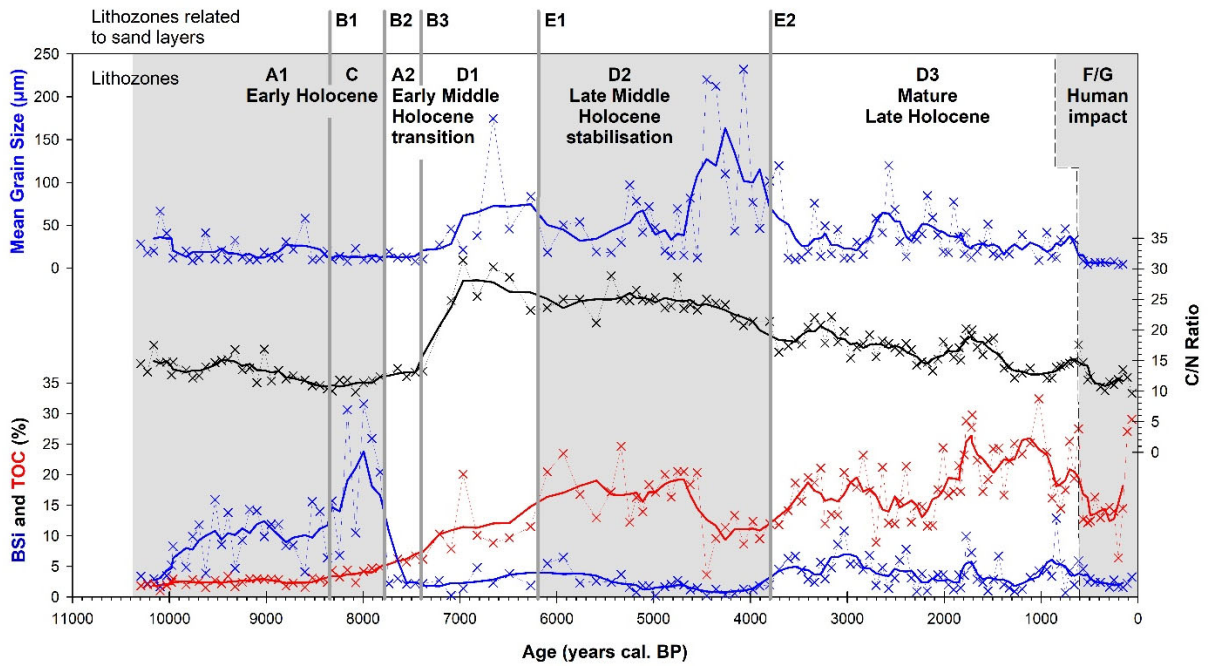
1308



1309

1310 Fig. 7: Age-depth relationship (red dotted line) modelled with “rbacon” and based on 21 radiocarbon  
 1311 dates (in blue) with the sediment surface (in green). The  $1\sigma$  error margins (gray dotted lines) are  
 1312 indicated as well as the five sand horizons (gray horizontal bars) excluded from age-depth model  
 1313 calculations.

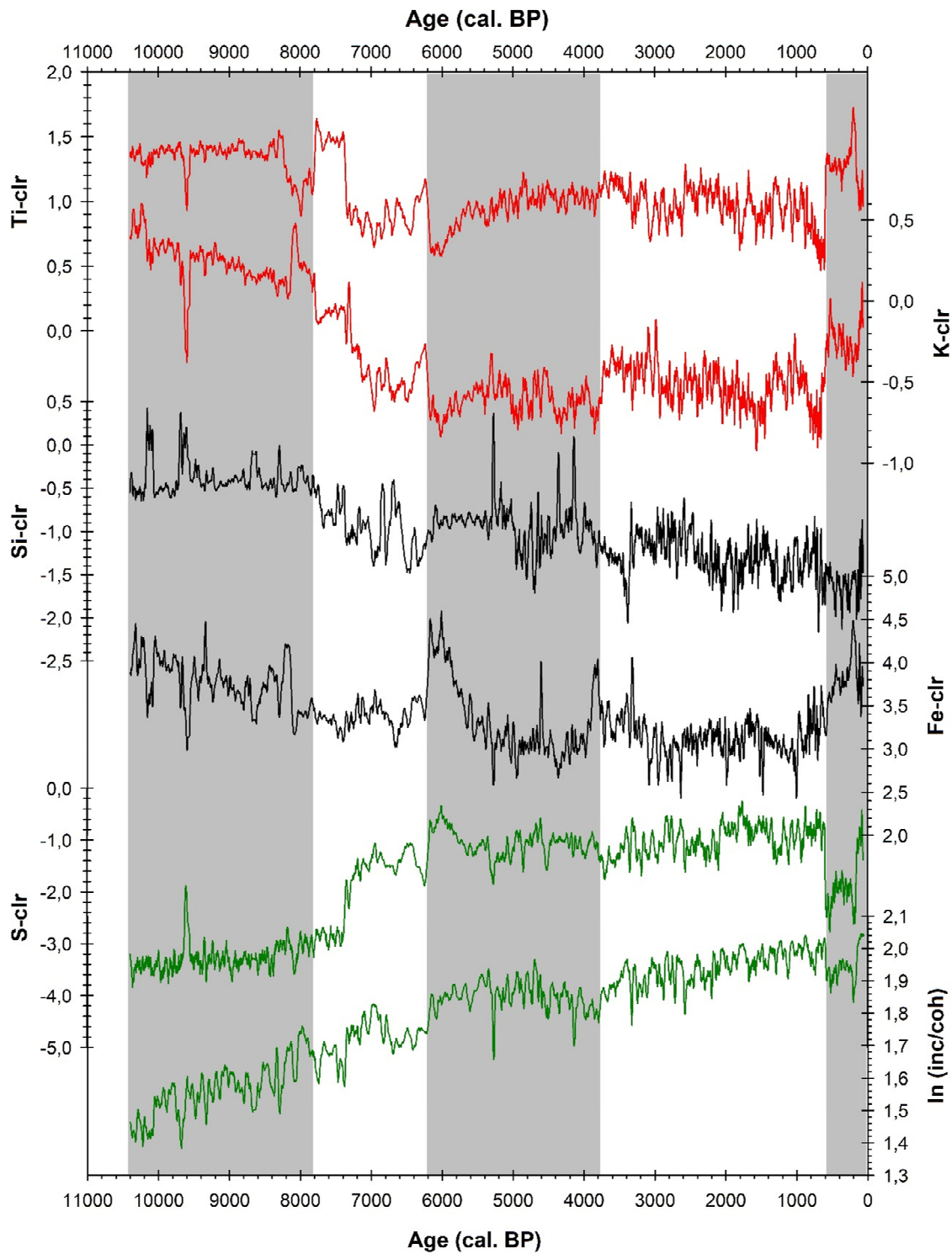
1314



1315

1316 Fig. 8: Selected geochemical data (biogenic silica: BSi; total organic carbon: TOC; carbon-to-nitrogen  
1317 ratio: C/N ratio) are shown together with mean grainsize vs. time. Lithozones and the position of  
1318 sand horizons (LZs B and E) excluded from age-depth modelling are labelled as well as stratigraphical  
1319 assignments and human impact.

1320

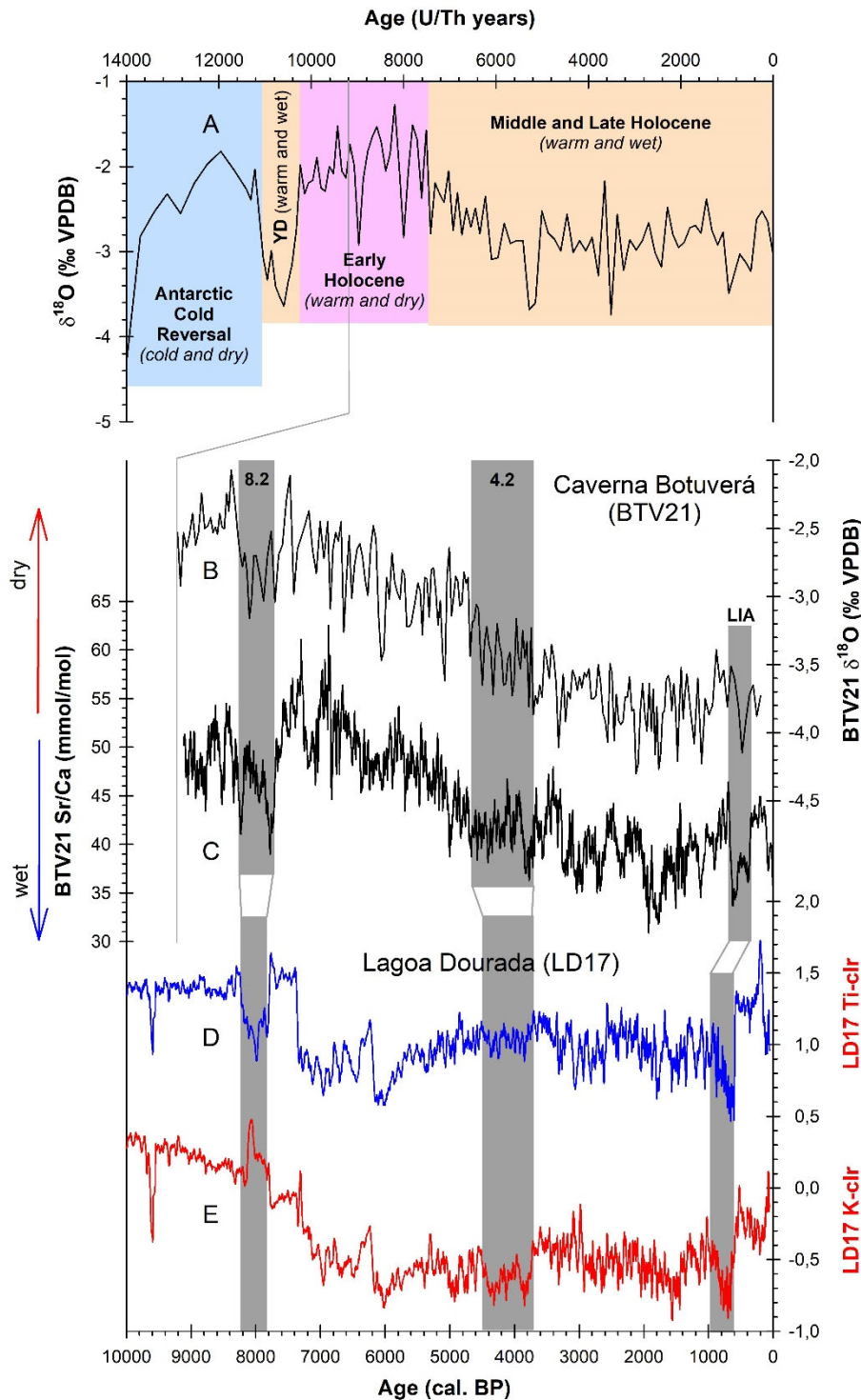


1321

1322 Fig. 9: Selected clr-transformed elemental data obtained by XRF core scanning. Shown are the  
 1323 elements sulphur (S), silica (Si), titanium (Ti), potassium (K), iron (Fe) and the incoherent/coherent  
 1324 ratio (inc/coh) vs. time. Shading as in Fig. 8.

1325

1326



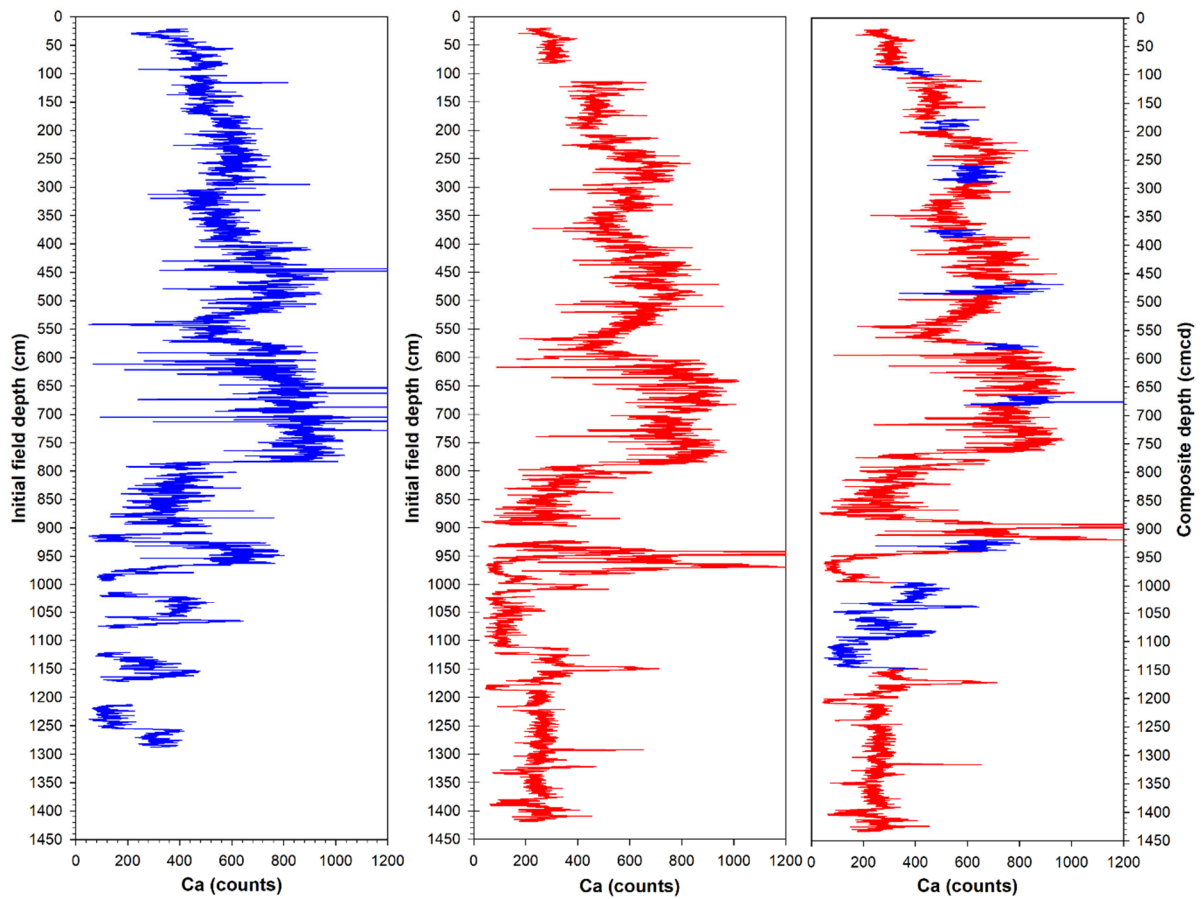
1327

1328 Fig. 10: Comparison of speleothem data from Caverna Botuverá with lacustrine sediment data from Lagoa  
 1329 Lagoa Dourada. A) Oxygen isotope record from Botuverá speleothem BTV2 focusing on the last 14 ka (Cruz, 2005;  
 1330 Cruz et al., 2005). Climatic conditions are labelled and color-coded (YD: Younger Dryas) and derived from  
 1331 Novello et al. (2017). Note that this time scale is in U/Th years! B) Oxygen isotope record and C) Sr/Ca ratio  
 1332 from Botuverá speleothem BTV21 for the Holocene (Bernal et al., 2016a; Bernal et al., 2016b) with  
 1333 hydroclimatic interpretation (arrows). Additionally, clr-transformed elemental data of D) titanium (Ti) and  
 1334 potassium (K) are shown from the sediment record of Lagoa Dourada. The three most prominent Holocene  
 1335 climatic events are marked by vertical gray bars. Note: the chronology for the last millennium of the Lagoa  
 1336 Dourada record is shown with the “rbacon” age-depth model causing a temporal offset for the last millennium  
 1337 – for explanation see the text. All data from Caverna Botuverá were accessed online via the NOAA  
 1338 Paleoclimatology Program on February 18, 2021.

1339 Tab. 1: Radiocarbon ages with sample depths, sample characteristics as well as reservoir corrections. Ages used for calculation of the reservoir effect are  
 1340 excluded from age-depth modelling (shaded in dark gray) as well as outliers mainly located in sand horizons (shaded in light gray).

Sample ID (LD-)	Lab. No.	Sampled Core	Section Depth (cm)	Composit Depth (mcd)	Type of Sample	Radiocarbon Age (BP)	± 1 σ	1 σ Range of Calibrated Radiocarbon Ages (cal. BP)	Reservoir Correction (yrs)	Comments
1	POZ-119117	LD17-B2	89.5-90.5	1,73	Macro-fossil	990	30	801-916		
2	POZ-111295	LD17-B3	29-30	2,05	Macro-fossil	1470	30	1300-1351		
3	UBA-29240	LD17-B5	6.8-6.9	3,87	Macro-fossil	2330	35	2156-2345		
4	POZ-121537	LD17-B6	41-42	5,18	Macro-fossil	3205	35	3357-3445		
5	POZ-119118	LD17-B7	56.2-56.6	6,34	Macro-fossil	4300	35	4730-4867		
6	POZ-107807	LD17-B8	39.1-39.2	7,16	Macro-fossil	4355	35	4839-4959		
7	POZ-122526	LD17-B8	53-54	7,30	Bulk	9700	40		5065	age used for reservoir correction with LD-8
8	POZ-119119	LD17-B8	54.1-54.5	7,31	Macro-fossil	4635	35	5145-5446		
9	POZ-119120	LD17-B8	55-56	7,32	Bulk	9870	40		5235	age used for reservoir correction with LD-8
10	POZ-122527	LD17-B8	102-103	7,79	Bulk	8530	50	3398-3821	5150±100	outlier; from sand horizon
11	POZ-119121	LD17-B9	10-11	7,94	Bulk	7930	50	2723-3134	5150±100	outlier; from sand horizon
12	POZ-116232	LD17-B9	43-44	8,27	Bulk	8330	40	3164-3558	5150±100	outlier; from sand horizon
13	POZ-122528	LD17-B9	79-80	8,63	Bulk	10590	50	5995-6383	5150±100	from sand horizon
14	POZ-119122	LD17-B10	41-42	8,92	Bulk	11630	60	7169-7555	5150±100	
15	POZ-111296	LD17-B10	64-65	9,15	Bulk	11380	60	6890-7265	5150±100	
16	UBA-29241	LD17-B10Liv	9.3-9.8	9,24	Macro-fossil	6235	35	7012-7163		
17	POZ-107808	LD17-B10Liv	82-83	9,98	Bulk	12020	60	7518-7840	5150±100	
18	POZ-119188	LD17-A11	29-30	10,02	Bulk	11620	50	7167-7485	5150±100	
19	POZ-107809	LD17-B11	96-97	11,49	Bulk	14540	80	10261-11083	5150±100	outlier; from sand horizon
20	POZ-116234	LD17-B12	42-43	11,85	Bulk	14660	80	10513-11083	5150±100	outlier
21	POZ-111297	LD17-B12	90-91	12,32	Bulk	12930	60	8373-8769	5150±100	
22	POZ-107810	LD17-B 13	76-77	13,15	Bulk	13750	70	9318-9889	5150±100	
23	POZ-107815	LD17-B 14	97-98	14,33	Bulk	13850	70	9486-10109	5150±100	
	POZ: Poznań Radiocarbon Laboratory, Poland									
	UBA: <sup>14</sup> Chrono Centre at Queen's University Belfast, Northern Ireland									

1341

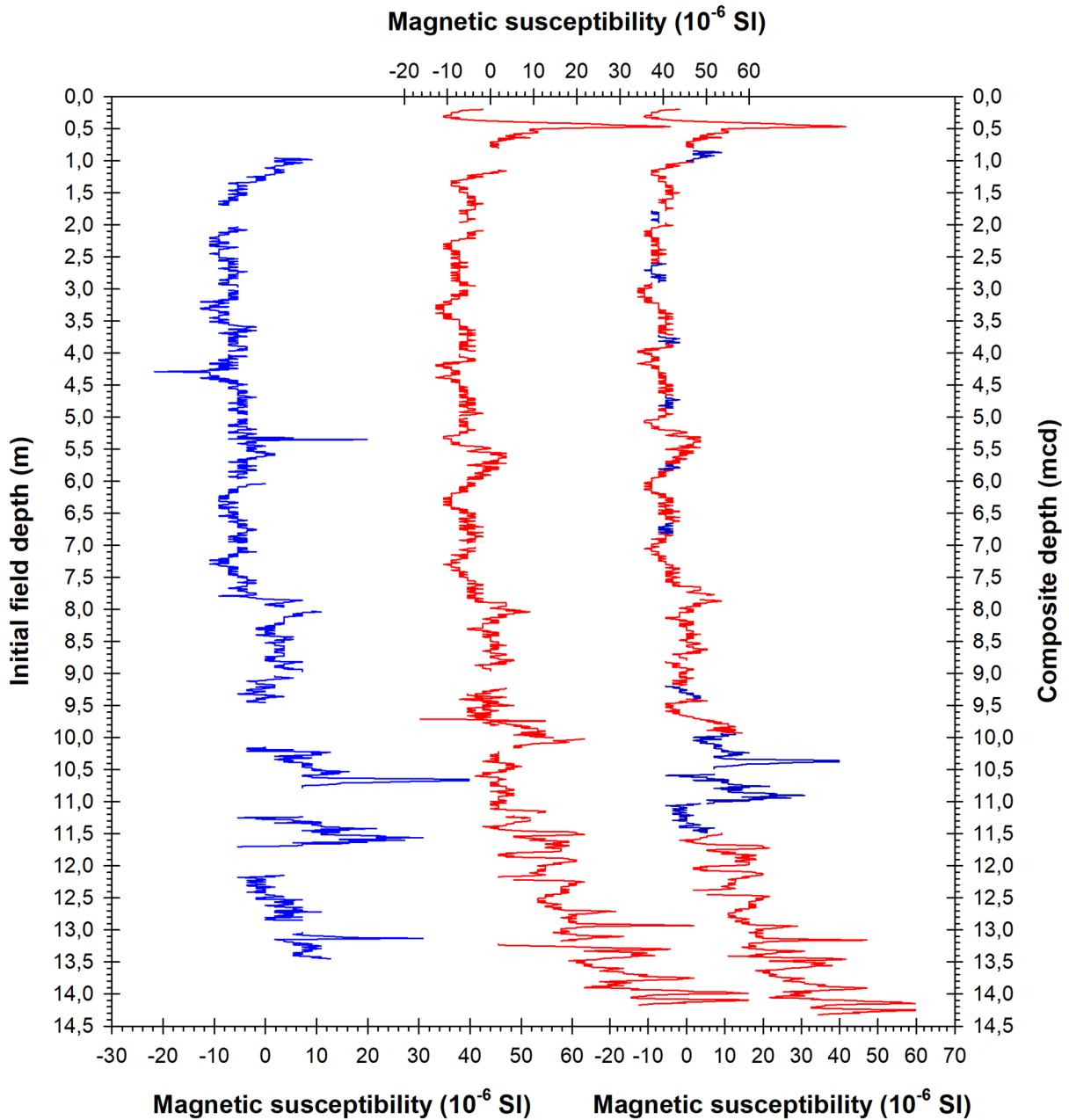


1342

1343 Fig. S1: Ca counts obtained by XRF core scanning vs. field depths for sediment cores LD17-A (blue)  
 1344 and LD17-B (red) as well as for the merged composite record, now on a composite depth scale and  
 1345 displayed in centimeter composite depth (cmcd).

1346





1347

1348

1349

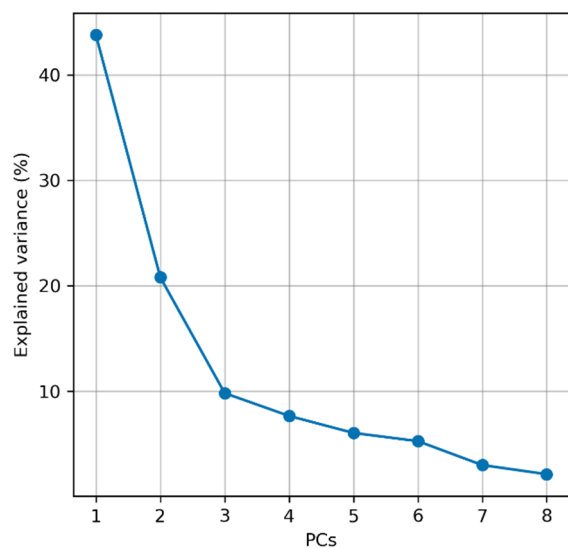
1350

1351

1352

1353

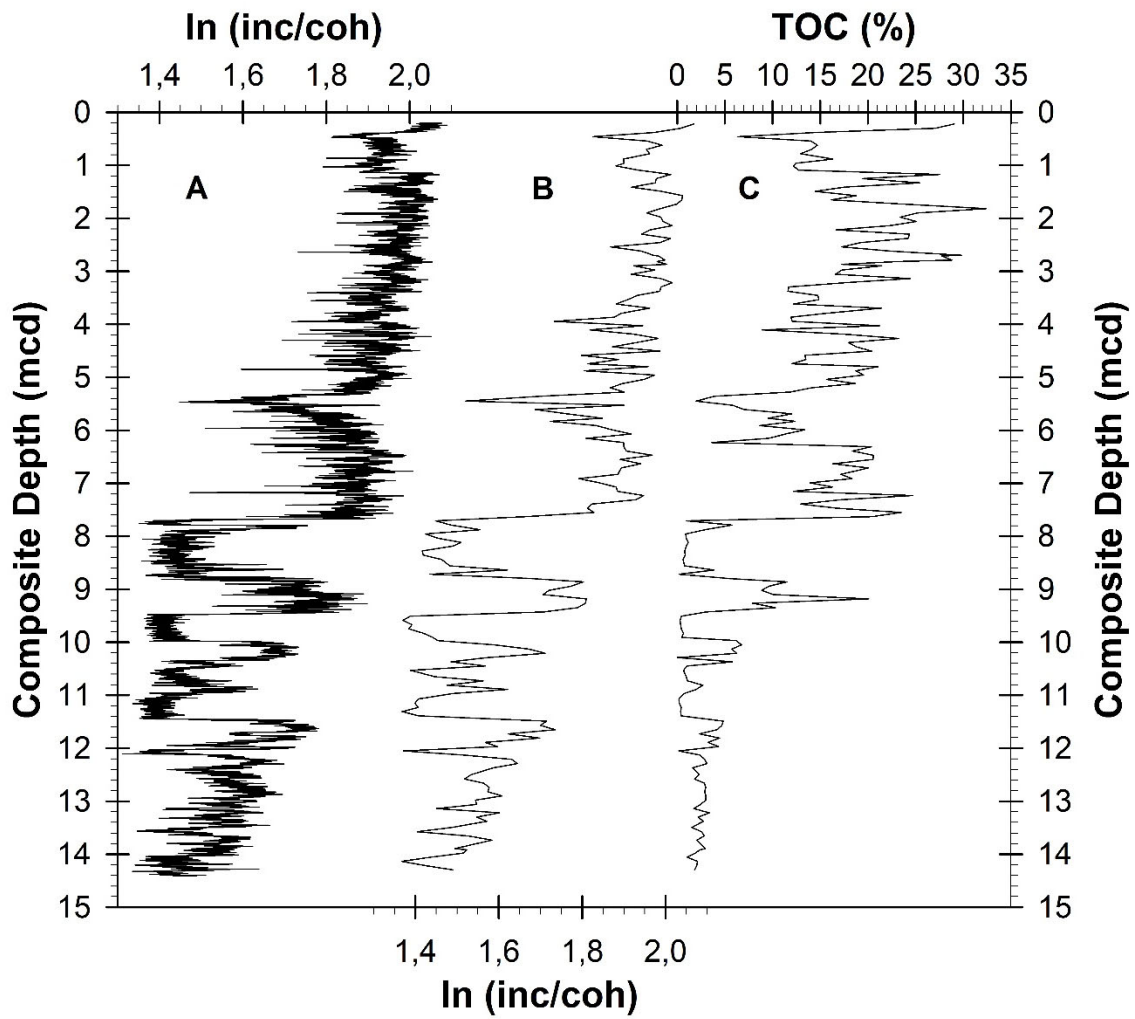
Fig. S2: Magnetic susceptibility versus field depths for sediment cores LD17-A (blue) and LD17-B (red) as well as for the merged composite record displayed on a composite depth scale in meter composite depth (mcd). Correlation of LD17-A and LD17-B is not based on the magnetic susceptibility data shown but on Ca data (cf., Fig. S1).



1354

1355 Fig. S3: Scree plot of the explained variance ratio for all principal components (PCs) based on  
1356 normalized (clr-transformed) and standardized elemental intensities obtained by XRF core scanning  
1357 (cf., Fig. 4).

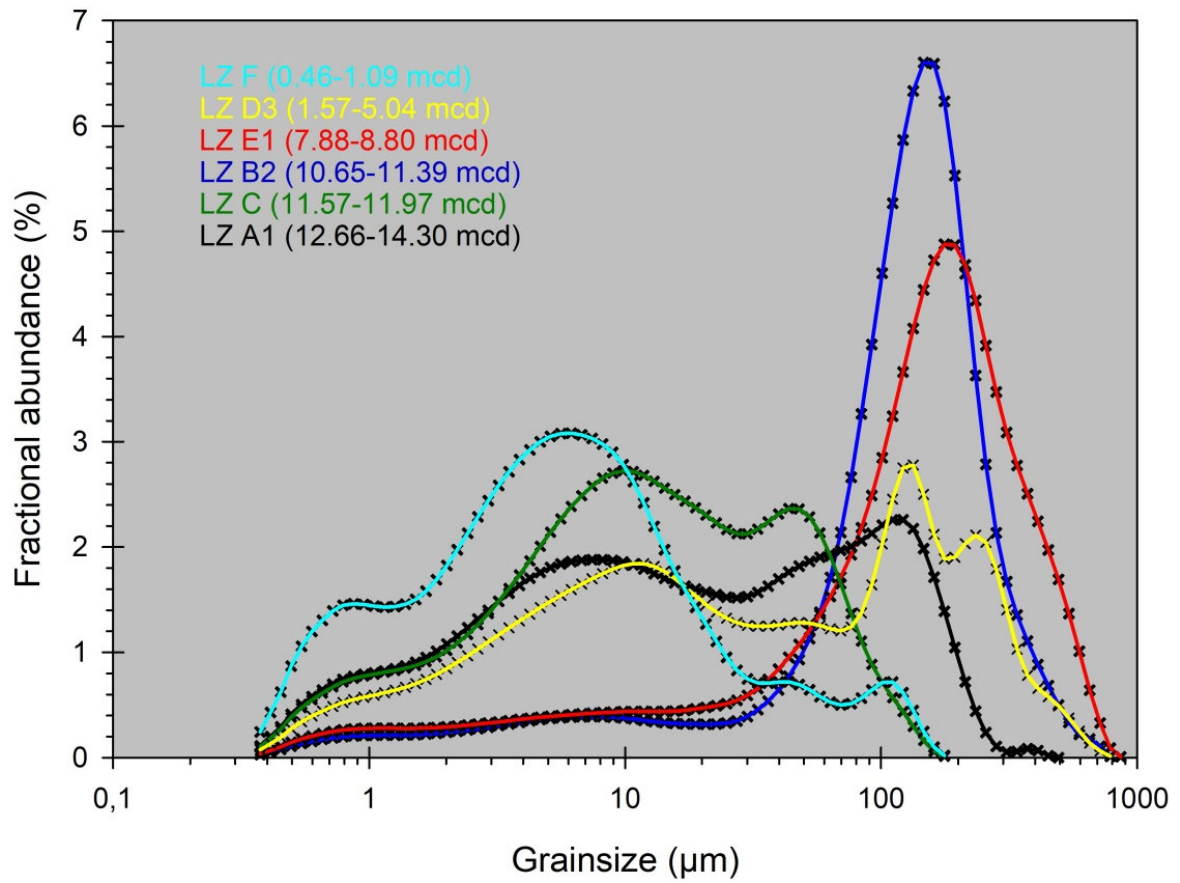
1358



1360

1361 Fig. S4: Organic matter for the sediment record from Lagoa Dourada. A) High resolution (2 mm)  
 1362 record of the ln inc/coh ratio; B) Same ratio with resolution reduced to 8 cm; C) Low resolution  
 1363 (8 cm) total organic carbon (TOC) record. Correlation between B and C:  $r = 0.88$ .

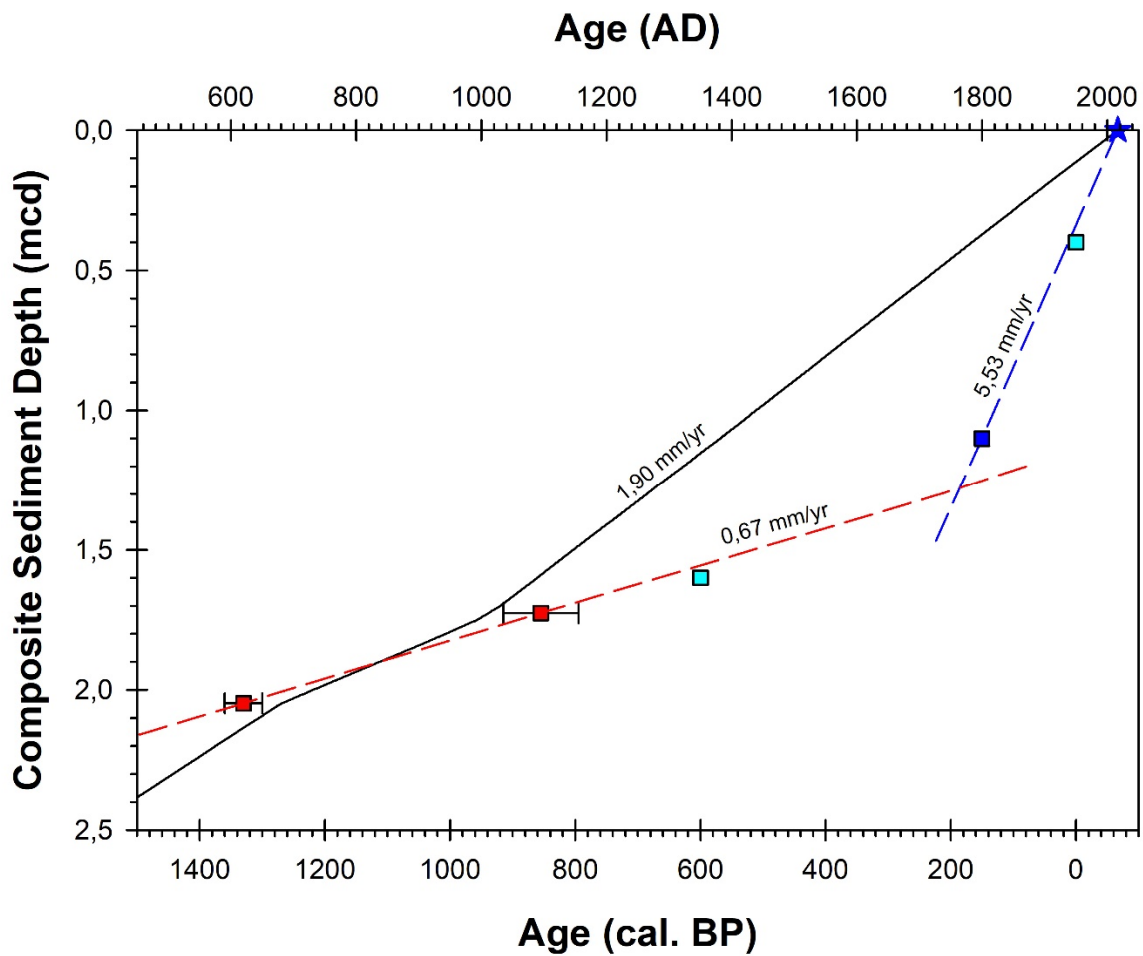
1364



1365

1366 Fig. S5: Grainsize frequency histograms of mean distributions for selected lithozones.

1367



1369

1370 Fig. S6: Modified chronology for the last 1500 years. On display are the “rbacon” age-depth model  
 1371 (black line), the two uppermost radiocarbon ages (red squares) with a linear sedimentation rate  
 1372 based on these two dates only (red dashed line) and an age for the onset of land-use change at AD  
 1373 1800 ±50 years (150 cal. BP; blue square) with a linear sedimentation rate (blue dashed line)  
 1374 calculated for this historical date and the sediment surface of the year of coring, i.e. AD 2017 (-63  
 1375 cal. BP) blue star). Values provided in mm/yr are respective linear sedimentation rates. Additionally, two  
 1376 data points are shown (cyan): (1) AD 1953 (-3 cal. BP) at 0.4 mcd, the year of establishing the Vila  
 1377 Velha State Park as indicated by returning organic sediments (onset of LZ G) coinciding with the  
 1378 calculated linear sedimentation rate; (2) The change in elemental data at 1.6 mcd interpreted as the  
 1379 onset of the LIA (see text for explanation) and its timing of AD 1300 (650 cal. BP) as based on linearly  
 1380 extrapolating the radiocarbon-based sedimentation rates.

1381

1382 Tab. S1: Correlation coefficients for 20 elements as well as incoherent (inc) and coherent (coh)  
 1383 radiation analyzed with the XRF core scanner for sediment cores LD-B6 (organic) and LD-B12  
 1384 (minerogenic). Both cores were 97 cm in length, scanned every 2 mm and consist of 486 individual  
 1385 data points. Each core scanning was repeated five times. Only elements with a high positive  
 1386 correlation of  $r > 0.8$  for at least one of the two core sections (shaded in gray) were selected for  
 1387 further statistical treatment.

LD-B6																							
Element	Al	Si	P	S	Cl	K	Ca	Ti	V	Cr	Mn	Fe	Ni	Cu	Zn	Br	Rb	Sr	Zr	Pb	Inc	Coh	
Mean counts for each element	35	149	17	135	7	217	1115	1248	24	74	28	9075	167	174	145	41	133	160	1044	43	51666	8473	
Correlation coefficient	0,052	0,956	0,037	0,994	0,037	0,941	1,000	0,997	0,183	0,360	0,350	0,999	0,273	0,396	0,860	0,158	0,523	0,519	0,981	0,127	0,995	0,902	
P value	0,288	<0,00001	0,6028	0	0,428	<0,00001	0	0	0,00003	<0,00001	<0,00001	0	<0,00001	<0,00001	<0,00001	0,00036	<0,00001	<0,00001	0	0,00311	0	0	
LD-B12																							
Element	Al	Si	P	S	Cl	K	Ca	Ti	V	Cr	Mn	Fe	Ni	Cu	Zn	Br	Rb	Sr	Zr	Pb	Inc	Coh	
Mean counts for each element	54	532	24	29	13	675	295	2043	25	53	34	21607	148	152	204	23	377	430	1687	102	39096	7919	
Correlation coefficient	0,094	0,978	-0,003	0,137	0,036	0,983	0,966	0,993	0,140	0,297	0,715	0,999	0,344	0,476	0,641	0,329	0,853	0,922	0,992	0,505	0,991	0,734	
P value	0,0321	0	0,4103	0,0019	0,2135	0	<0,00001	0	0,00098	<0,00001	<0,00001	0	<0,00001	<0,00001	<0,00001	<0,00001	<0,00001	<0,00001	<0,00001	0	<0,00001	0	<0,00001

1388

1389